Setup to build a fluorescent protein laser based on Förster resonance energy transfer and the construction of a 515 nm pump laser

OSCAR FRICK

Master of Science Thesis
Stockholm, Sweden 2014

Laser Physics
Department of Applied Physics
KTH - Royal Institute of Technology
106 91 Stockholm
Sweden

TRITA FYS 2013:33
ISSN 0280-316X
ISRN KTH/FYS/-13:33-SE

Tryck: Universitetsservice US AB

Abstract

In this master thesis project, the possibility of constructing a Venus yellow fluorescent protein dye laser in a cavity designed to manage Förster resonance energy transfer lasing have been investigated. The three main parts of the project was to synthesize Venus yellow fluorescent protein, construct a 515 nm, pulsed, pump laser, and design, as well as construct, a laser cavity designed to manage Förster resonance energy transfer lasing.

The proteins were synthesized using a well established method with E. coli grown in NZYM broth. To release the proteins from the bacteria, sodium dodecyl sulfate was used, followed by centrifuging to separate the proteins from cell residue. Spectral analysis confirmed successful synthesis and lysis of the proteins. Fluorescence correlation spectroscopy was used to determine the protein concentration to 30 nM, though comparing absorption at 515 nm with the measured concentration suggested low purity of the protein solution.

The 515 nm pump was generated from an Yb:KYW solid state laser, locked to emit at 1030 nm using a volume Bragg grating. The 1030 nm laser was pulsed using passive q-switching with a Cr:YAG crystal. It was extra-cavity frequency doubled using periodically polarized KTP, generating a 515 nm pulsed output with a 200 ns FWHM pulse length and a repetition rate of about 8.6 kHz. The repetition rate was lowered to 86 Hz using a tuned chopper with a 1% throughput. During the construction of the pump laser, it was found that the damage threshold of KTP when using these medium long pulses was drastically lowered to about 33 MW/cm^2. Although it has been previously suggested that this is an effect of gray-tracking, the use of the less gray-tracking prone rubidium doped KTP did not improve the damage threshold.

The Venus yellow fluorescent protein laser cavity used a volume Bragg grating, with a FWHM bandwidth of 0.4 nm and reflection peak at 533.2 nm, both as input and output coupler. The grating was angularly tuned to reflect at 530 nm. The Venus yellow fluorescent protein solution used as gain medium was held in the cavity using two sapphire plates, which were placed in Brewster angle, giving a total gain medium length of about 4.6 mm. On one side of the grating a plane mirror was used to close the cavity, on the other side a R = 200 mm mirror and a R = 25 mm mirror was placed, having the Venus yellow fluorescent protein between them, giving a collimated beam incident on the volume Bragg grating.

The Venus yellow fluorescent protein never achieved lasing using this setup, most probably because of the low concentration and low purity of the gain material solution.

Sammanfattning

Detta examensarbetesprojekt har undersökt möjligheten att konstruera en färgämneslaser med det gult fluorescerande proteinet Venus YFP som lasermedium, i en kavitet konstruerad för att hantera lasring med Förster-resonant energiöverföring. De tre huvuddelarna i examensarbetet var att syntetisera proteinerna, konstruera en 515 nm pulsad pumplaser samt att designa och konstruera en laserkavitet som hanterar lasring med Förster-resonant energiöverföring.

Proteinerna syntetiserades med en etablerad metod där E. Coli läts växa i NZYM-buljong. För att släppa lös proteinerna från cellerna användes natriumdodecylsulfat, följt av centrifugering för att separera proteinerna från cellresterna. Spektralanalys visade att syntetiseringen såväl som lössläppningen av proteinerna var lyckad. Fluorescenskorrelationsspektroskopi användes för att mäta koncentrationen till 30 nM, dock visade en jämförelse med ljusabsorption vid 515 nm på låg renhet i proteinlösningen.

Pumplasern genererades från en kristallaser med Yb:KYW som gainmaterial, låst till 1030 nm med hjälp av ett volymbraggitter. Pulser erhölls med tekniken passiv Q-växling med hjälp av en Cr:YAG-kristall som mättnadsbar absorbator. Den var extrakavitärt frekvensdubblad till 515 nm med periodiskt polad KTP. Pulsen hade en halvvärdesbredd på ungefär 200 ns och en repetitionsfrekvens på ca. 8,6 kHz, något som sänktes ytterligare, till ungefär 86 Hz med en 1% chopper. Vid konstruktionen av pumplasern upptäcktes att skadetröskeln för KTP sänktes drastiskt, till ungefär 33 MW/cm^2, vid användning av våra mediumlånga pulser. Det har tidigare föreslagits att detta beror på gråspårning, men användande av rubidium-dopat KTP tillförde ingen förbättring, trots att rubidium-dopat KTP är mindre känsligt för gråspårning.

Kaviteten för att få Venus YFP att lasra använde ett volymbraggitter med en halvvärdesbandbredd på 0.4 nm och en reflektionstopp på 533.2 nm, både som inkopplings- och utkopplingsselement. Gittret sattes i vinkel för att reflektera vid 530 nm. Proteinlösningen, det vill säga lasermediet, hölls på plats med två safirplattor placerade i Brewstervinkel. Lasermediets totala längd i denna uppställning var ca. 4,6 mm. På ena sidan av gittret användes en plan spegel för att stänga kaviteten, på andra sidan användes en spegel med kurvaturradie 200 mm samt en spegel med kurvaturradie 25 mm. Lasermediet placerades mellan dem, vilket gav en kollimerad stråle vid gittret.

Lasring uppnåddes aldrig med denna uppställning, detta beror med största sannolikhet på grund av den låga koncentrationen och låga renheten hos proteinlasermediet.

Acknowledgements

I would like give sincere thanks to my supervisor, Staffan Tjörnhammar. Not only has he supplied me with laboratory equipment, but has also worked close with me during the whole process and has taught me the practical aspects of designing and constructing lasers.

I would like to express my gratitude to Sergey Zelenin and Marina Zelenina, who have assisted me with the biological part of the work. They have both contributed greatly to being successful in synthesizing the proteins needed.

I am grateful towards Otto Manneberg, prof. Jerker Widengren and Stefan Wennmalm who has assisted me in doing measurements of above mentioned proteins. They have also given me many valuable hints and tips about how to draw conclusions and extract data from the measurements.

I am thankful to prof. Fredrik Laurell, prof. Valdas Pasiskevicius and prof. Hjalmar Brismar for letting me do this project.

Last, and certainly no least, I would like to express my deepest thanks to the laser physics research group at AlbaNova University Center. I have been welcomed in the warmest manner and every member of the group have contributed to this project in one way or another.

List of symbols and abbreviations

η	Transfer efficiency
Λ	Volume Bragg grating grating period
λ	Wavelength
σ_{12}	Absorption cross section
σ_{21}	Emission cross section
$\omega_{e^{-2}}$	Focused beam radius
Amp	Ampicillin
AR coating	Anti Reflective coating
BFP	Blue Fluorescent Protein
CFP	Cyan Fluorescent Protein
Cr:YAG	Chromium doped yttrium aluminum garnet
CW	Continuous Wave operation of a laser
E. coli	Escherichia coli
eCFP	Enhanced Cyan Fluorescent Protein
eGFP	Enhanced Green Fluorescent Protein
eYFP	Enhanced Yellow Fluorescent Protein
F	Photon flux
FCS	Fluorescence Correlation Spectroscopy
FRET	Förster Resonance Energy Transfer
FWHM	Full Width Half Maximum
$G(\tau)$	Autocorrelation function of a fluorescence correlation spectroscopy
GFP	Green Fluorescent Protein
k_B	Boltzmann's constant
KTP	$KTiOPO_4$, potassium titanyl phosphate
LBO	Lithium triborate
M^2	Beam quality parameter
N_a	Avogadro's constant
N_X	Population densities of energy level X
n_0	Bulk refractive index
OSA	Optical Spectrum Analyzer
PPKTP	Periodically Polarized potassium titanyl phosphate
PP-RKTP	Periodically Polarized rubidium doped potassium titanyl phosphate
RKTP	Rubidium doped potassium titanyl phosphate
RPM	Revolutions Per Minute
SDS	Sodium Dodecyl Sulfate
SHG	Second Harmonic Generation
T	Temperature
V_{con}	Confocal measurement volume
VBG	Volume Bragg Grating
W_{12}	Stimulated emission rate
W_{21}	Absorption rate
Yb:KYW	Ytterbium doped potassium yttrium tungstate
YFP	Yellow Fluorescent Protein

Contents

Chapter 1

Introduction

This chapter gives a short introduction to the project. 'Background' describes why this research subject is of interest, 'The aim of this thesis' being just that, and 'Thesis outline' giving a description to the layout of this thesis.

1.1 Background

The research area of lasing in biological proteins is a relatively new subject. However, with recent demonstration of lasing from Green Fluorescent Protein (GFP) in a solution and, more importantly, lasing from a single cell induced with GFP [1], it is of great interest to the biological sciences to investigate matters of protein lasing further.

A straight forward example of what might be possible to achieve with single cell lasing is hyper sensitive detection of ions inside cells. Ions, as well as other cell components, are common to detect and image using fluorescent molecules. The way this is done is to attach the fluorescent molecules to the cell components wished to examine using antibodies as a middle hand. Antibodies are special proteins that naturally appear in the immune system, and they are designed to connect to two different biological structures. In the immune system antibodies are used to tag harmful objects, such as intruding bacteria or viruses, by attaching one of its ends to the harmful object, while the other end is "designed" to attach to parts of the immune system that will fight the harmful object.

In cell labeling this is exploited by first exposing the cell interior to antibodies that has one end designed to attach to the cell component wished to examine, and the other end designed to attach to the fluorescent particle going to be used. The cell interior is then exposed to the fluorescent protein, which will attach to the antibodies, which in turn will already be attached to the cell component that is going to be examined. Imaging of the cell is then done using a fluorescence microscope. With small concentrations of such ions inside a cell it might be very hard, or even impossible, to distinguish the fluorescence signals from the background

noise. By introducing a resonance cavity and employing the sample in a laser, the signal would be directed into the microscope, which would greatly improve the light economy.

Another possibility would be an improvement of Förster Resonance Energy Transfer (FRET) microscopy. FRET microscopy is a type of fluorescent microscopy where a dipole-dipole coupling between two fluorescent proteins is used to transfer energy from one fluorophore to the other [2], a coupling which has a very strong dependence of the distance between the two particles interacting. By pumping only the fluorophore emitting the higher energy photons (called the donor fluorophore) and introducing optical systems to separate the wavelengths emitted by the two different fluorophores, it is possible to measure only the other fluorophore's emission (called the acceptor fluorophore). What this system does is measure when two different fluorophores are in proximity of each other.

Doing labeling of different cell components with two different fluorophores that form a FRET pair makes it possible to measure and picture intracellular interactions [3]. However, this technique introduces problems with output light intensity, and often the output signal is comparable to the noise levels of the system [4]. If it would be possible to achieve lasing in a FRET system, this might very well solve this problem for a lot of FRET microscopy applications.

1.2 The aim of this thesis

In particular, this thesis project is aimed at investigating the possibility of lasing in a FRET system. More specifically, the aim has been to investigate if it is possible to construct a dye laser from the Venus Yellow Fluorescent Protein (Venus YFP) in a cavity designed for FRET lasing, using a protein solution that has been synthesized locally at AlbaNova University Center.

To do this, three partial goals have been identified. A protein solution needs to be synthesized locally at AlbaNova University Center and evaluated as a laser gain medium. A pump laser suitable for pumping the synthesized fluorescent protein needs to be designed, constructed and evaluated. Lastly, a laser cavity that can manage FRET lasing needs to be designed and built.

1.3 Thesis outline

In chapter 2 some basic laser theory needed in order to fully compromise all information in this thesis is presented. Due to the nature of this thesis the chapter is focused on the theory surrounding laser gain materials and what properties are needed in order to successfully use them to achieve lasing.

Chapter 3 describes fluorescent proteins, their function as a gain material, as well as presenting the results from the evaluation of the fluorescent proteins that were synthesized and used during this project.

Chapter 4 is dedicated to describing the pump laser design, construction and properties.

In chapter 5 the fluorescent protein laser is presented and evaluated.

In chapter 6 the conclusions and possible extensions of the project are presented.

Chapter 2

Basic laser and volume Bragg grating theory

This chapter describes some basic theory and functions of lasers and volume Bragg gratings that needs to be known in order to fully acquire the information in this thesis.

2.1 The laser concept

The basic laser concept is to have light amplification by a phenomenon known as stimulated emission. Stimulated emission is, simply put, the fact that an atom (or molecule) in an excited state might release its excess energy in form of a photon given that another photon travel close enough to interact with it. In order to stimulate emission from an excited molecule, the photon need to have the same energy as the energy gap between the excited and the relaxed energy state of the atom, in which case the atom will release its energy in form of photon. A simple illustration of the phenomenon is presented in Fig. 2.1, and exactly as the illustration suggests the photon emitted from the excited atom will have the same wavelength, direction, phase and polarization as the stimulating photon.

The light amplification is practically achieved by having a set of mirrors and an optical gain material set up to form an optical resonator, which means that the components should be aligned so that there is periodic refocusing of the light. Using ray approximations and ray matrix calculations, it is possible to determine whether or not a certain setup of mirrors and gain material will form an optical resonator [5, 6]. However, just having the parts form an optical resonator is not enough, the gain material also needs certain properties. Since these properties are of special importance when investigating a new gain material they are discussed in further detail in Sec. 2.2.

With all demands fulfilled, the optical resonator will be filled with photons trapped between the mirrors, stimulating emission of more photons from the gain

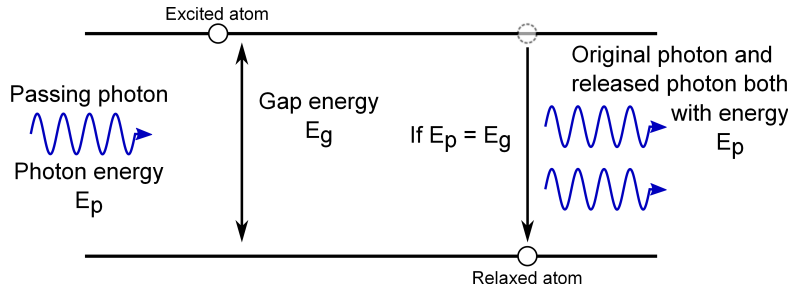

Figure 2.1: Schematic showing a simple example of stimulated emission. An incident photon passes an excited atom, which has a high probability of releasing its surplus energy as an additional photon with the same optical properties as the incident photon.

material. In order to utilize this light, one of the mirrors, known as output coupler, is made with a reflectivity less than 100% as to let some of the photons through. This light, that have leaked out through the output coupler, is what forms the laser beam. In most applications, this is the light that is useful.

2.2 Gain material and population inversion

The gain material is what provides the optical resonator with the necessary excited atoms (or molecules) to have stimulated emission and thus achieving lasing. However, since every photon emitted from the gain material will relax one of the atoms, which will then not be able to provide any more photons, it is apparent that the atoms in the gain material needs to be re-excited in order to provide any considerable light amplification. This process, known as pumping, can be done in several ways depending on what material is used.

The two most common ways to add energy to a gain material is either through electrical or optical pumping. In electrical pumping, the gain material is exposed to a current, and, in optical pumping, the gain medium is irradiated by light which is absorbed by the gain material. Both of these pump methods are governed by the same physical rules, but for simplicity reasons we will only consider the case with an optical pump. The simplest pumping scheme imaginable is having a two-level system, as shown in Fig. 2.2. In a two-level system, the atoms are optically pumped to their excited states by absorbing a photon each, and then relaxed down by stimulated emission, emitting a photon each with the same energy as the photon used to pump the atom in the first place. What will be shown now is that this system, however convenient and simple it seems, can never achieve lasing.

Imagine an atom whose electron is situated in its excited energy state. It is apparent that this electron will, sooner or later, fall down to its relaxed energy state. Upon relaxation of the excited electron, the energy dispatched can take

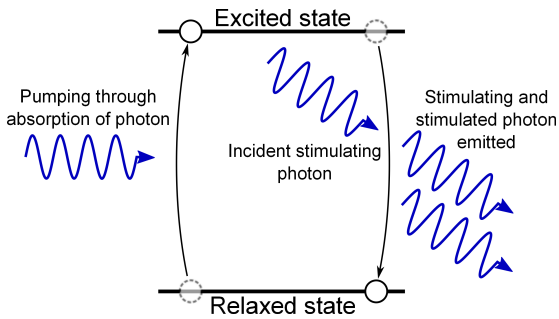

Figure 2.2: Pumping scheme for a two level stimulated emission system. An external optical source is used to excite an atom or molecule, which can then be stimulated to release its excessive energy in the form of a photon.

one of several different shapes. The relaxation can be non radiative, in which the energy is released into the surroundings by atom movement, collisions, phonons, or similar, depending on what type of material the relaxation takes place in. The energy can spontaneously be converted to an emitted photon, which is what is called spontaneous emission. Lastly, if there is an external stimulating photon, the electron can be relaxed through stimulated emission.

From a laser perspective, the stimulated emission is of most interest. The non-radiative emission will not contribute to a light amplification at all, and the spontaneous emission will have a random emission direction and thus the contribution from the spontaneous emission will be neglectable. What we must also consider, however, is the absorption of light. The stimulated emission rate is only dependent on the number of excited atoms per unit volume, and the absorption rate is only dependent on the number of relaxed state atoms per unit volume. They can be described mathematically as

$$\left(\frac{\mathrm{d}N_2}{\mathrm{d}t}\right)_{\text{stim. em.}} = -\left(\frac{\mathrm{d}N_1}{\mathrm{d}t}\right)_{\text{stim. em.}} = -W_{21}N_2 \tag{2.1}$$

$$\left(\frac{\mathrm{d}N_1}{\mathrm{d}t}\right)_{\text{absorption}} = -\left(\frac{\mathrm{d}N_2}{\mathrm{d}t}\right)_{\text{absorption}} = -W_{12}N_1 \quad , \tag{2.2}$$

where N_2 and N_1 is the population density in their respective energy levels, and W_{21} and W_{12} are the rates of the stimulated emission and the absorption respectively. Both W_{21} and W_{12} are proportional to the photon flux, F. The proportionality factors are usually denoted σ_{21} and σ_{12}, they are called the emission and absorption cross-sections respectively. Equations 2.1 and 2.2 can then be rewritten to

$$\left(\frac{\mathrm{d}N_1}{\mathrm{d}t}\right)_{\text{stim. em}} = \sigma_{21}FN_2 \tag{2.3}$$

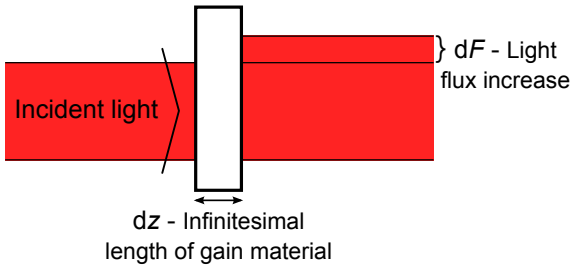

Figure 2.3: Graphical representation of dF.

$$\left(\frac{\mathrm{d}N_2}{\mathrm{d}t}\right)_{\text{absorption}} = \sigma_{12} F N_1 \quad . \tag{2.4}$$

To investigate if a certain material gives gain or loss, imagine a material of length dz that has the excited and relaxed population densities as N_2 and N_1 respectively. This material is subject to an incident beam with photon flux, F, and we want to quantify the difference, dF, between the incident beam flux and the emitted beam flux (illustrated in Fig. 2.3). Atoms being relaxed through stimulated emission will add to both the photon flux difference dF, and to the relaxed population density N_1. Atoms being excited through absorption will subtract from the photon flux while adding to the excited state population. Then it is apparent that

$$\frac{\mathrm{d}F}{\mathrm{d}z} = \left(\frac{\mathrm{d}N_1}{\mathrm{d}t}\right)_{\text{stim. em.}} - \left(\frac{\mathrm{d}N_2}{\mathrm{d}t}\right)_{\text{absorption}} = F(\sigma_{21} N_2 - \sigma_{12} N_1) \quad , \tag{2.5}$$

i.e., the flux difference per length is the stimulated emission rate minus the absorption rate.

If it is assumed that N_2 and N_1 are non-degenerate energy sub-levels it can be shown that $\sigma_{21} = \sigma_{12} = \sigma$, which yield that

$$\frac{\mathrm{d}F}{\mathrm{d}z} = \sigma F(N_2 - N_1) \quad . \tag{2.6}$$

With a more detailed model that assumes that N_2 and N_1 has g_2 and g_1 degenerate energy sub-levels respectively, this no longer applies. Instead the relation will be $g_2\sigma_{21} = g_1\sigma_{12}$, from which we can rewrite Eq. 2.5 to

$$\frac{\mathrm{d}F}{\mathrm{d}z} = F\sigma_{21}\left(N_2 - \frac{g_2}{g_1} N_1\right) \quad . \tag{2.7}$$

According to this relation, in order to have light amplification (dF/dz>0), it is needed that

$$N_2 > \frac{g_2}{g_1} N_1 \quad . \tag{2.8}$$

When this relation is fulfilled, it is said that population inversion is achieved, a necessary condition to have lasing in a medium.

Without any external stimulus, the populations of the energy states will be described by Boltzmanns law. However, when degenerate energy levels are taken into account, the law will be slightly different compared to when they are not taken into account. With a total population density of N_2 and N_1 in the excited and relaxed states, the population density of each separate degenerate sublevel will be N_2/g_2 and N_1/g_1. Boltzmanns law applies to all these sublevels separately[6], that is

$$\frac{\frac{N_2}{g_2}}{\frac{N_1}{g_1}} = e^{-\frac{E_2-E_1}{\mathrm{k_B}T}} \quad , \tag{2.9}$$

where E_2 and E_1 are the energy levels associated with the excited and relaxed state respectively, $\mathrm{k_B}$ is Boltzmanns constant and T is the temperature in kelvin. From this it is easily seen that

$$N_2 = N_1 \frac{g_2}{g_1} e^{-\frac{E_2-E_1}{\mathrm{k_B}T}} \quad , \tag{2.10}$$

since $E_2 > E_1$ it is realized that

$$N_2 < \frac{g_2}{g_1} N_1 \quad . \tag{2.11}$$

This means that in thermal equilibrium, we will never have population inversion.

Now, imagine wanting to pump a two level system (such as the above) to reach population inversion. Starting out with a material that in thermal equilibrium acts as an absorber will decrease the difference between the population up to a point where

$$N_2 = \frac{g_2}{g_1} N_1 \quad . \tag{2.12}$$

At this point, according to Eq. 2.6, we will not have any flux difference before and after passing through a material. Optically, the material behaves as it is totally transparent. Since it does not absorb any net energy at this state, the material cannot be pumped to population inversion. This applies for any transitions back and forth between two states, and thus we can conclude that we must have a more complex pumping scheme than a two-level system to be able to have lasing.

2.2.1 The four level system

With a rigorous proof that it is impossible to achieve lasing using a two-level system it is apparent that a more complex pumping schematic is needed to achieve lasing. One example of such a system is the four-level system, which also happen to be a common pumping scheme amongst modern lasers. A sketch of a four-level system

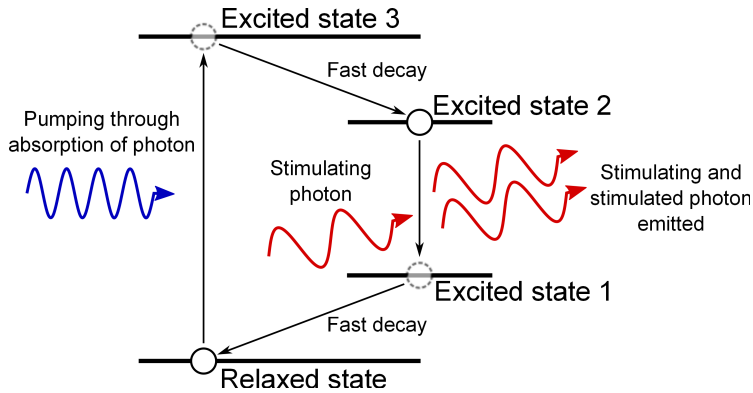

Figure 2.4: Sketch of a four-level laser system. There is pumping from the relaxed state up to the highest excited state, from which there is fast (non-radiative) decay down to the state from which stimulated emission is possible. After the simulated emission there is also fast decay back down to the relaxed state. Note that the pump light has higher photon energy than the laser light.

is presented in Fig. 2.4, where, as can be seen, the pump excites atoms from their ground states to the most energetic state involved in the lasing system. From that point there should, ideally, be an infinitely fast decay down to the higher state that is associated with the stimulated emission. The next relaxation is the radiative transition, and will be where we use the stimulated emission to achieve light amplification, and the last relaxations should also, ideally, be an infinitely fast decay back to the original, relaxed, state. All states are also separated by an energy that is large compared to $\mathrm{k_B}T$.

Understanding that this system can achieve lasing is done through qualitative reasoning and the previously presented equations. First we conclude that, since all energy levels are separated by energies that are large compared to $\mathrm{k_B}T$, only the ground state will have any population present in thermal equilibrium. Furthermore, with the knowledge that the above presented equations are valid for transitions between any two energy levels, it can be concluded that this system will be optically transparent for photons with energy corresponding to the energy gap between the first and second excited states when there is no external pumping present. This because populations at both levels are zero ($N_2 = N_1 = 0$).

We now imagine applying an external pump that starts rising molecules from the relaxed state up to the third excited state. The excited molecules will immediately be relaxed down to the second excited state, from which they will be able to radiate when decaying down to the first excited state. Since the population in the first excited state is still zero, according to Eq. 2.8, we have population inversion (since $N_1 = 0 < N_2$). Moreover, because the relaxed molecules will be subject to a fast

decay down to the relaxed state, the first excited state will never be populated, and so, as long as there is any pumping of the gain material there will be population inversion between the second and first excited state and lasing is possible.

2.3 Reflecting volume Bragg gratings

The Volume Bragg Grating (VBG) is a component made out of dielectric material with periodic alternations of refractive index. In essence, a reflecting VBG can be thought of as a mirror that is highly reflecting for wavelengths meeting the Bragg condition and transparent for all other wavelengths. The Bragg condition is

$$\lambda_R = 2n_0\Lambda\cos\theta_0 \quad , \tag{2.13}$$

where λ_R is the reflected wavelength in vacuum, n_0 is the bulk material refractive index, Λ is the grating period and θ_0 is the angle between the normal of the grating structure and the incident light internally in the VBG bulk.

Looking at the Bragg condition it is apparent that it is possible to change the reflected wavelength by altering the incident angle on the VBG, the physical explanation being that a change of incident angle alters the modulation period experienced by the incident light. Another effect of the incident angle dependence is that a too focused beam (a beam with too large angular divergence) will not be completely reflected. Photons with an oblique normal incidence angle will be subject to a longer grating period than photons with no normal incidence angle, and thus may not be reflected.

A reasonable rule of thumb limit for when a plane wave approximation is applicable for an oblique incidence angle on a VBG is [7]

$$\frac{\pi}{4}n_0\frac{\omega_{e^{-2}}}{\lambda_B^2}\Delta\lambda > \sin\theta_0 \quad , \tag{2.14}$$

where $\omega_{e^{-2}}$ is the focus beam radius, λ_B is the wavelength where the VBG has its reflectivity peak and $\Delta\lambda$ is the zero-to-zero bandwidth of the VBG.

However, knowing the internal incidence angle on the grating structure is tricky. Instead it can be calculated from the Bragg condition (Eq. 2.13), from which it can be seen that the internal incidence angle is

$$\theta_0 = \cos^{-1}\left(\frac{\lambda_R}{2n_0\Lambda}\right) \quad , \tag{2.15}$$

where λ_R denotes the wavelength that is reflected. The grating period, Λ, is easy to calculate from the Bragg condition for normal incidence angle:

$$\Lambda = \frac{\lambda_B}{2n_0} \quad . \tag{2.16}$$

Inserted into Eq. 2.15 this gives

$$\theta_0 = \cos^{-1}\left(\frac{\lambda_R}{\lambda_B}\right) \quad , \tag{2.17}$$

which inserted into Eq. 2.13 gives

$$\frac{\pi}{4} n_0 \frac{\omega_{e^{-2}}}{\lambda_B^2} \Delta\lambda > \sin\left\{\cos^{-1}\left(\frac{\lambda_R}{\lambda_B}\right)\right\} = \sqrt{1 - \left(\frac{\lambda_R}{\lambda_B}\right)^2} \quad , \quad \frac{\lambda_R}{\lambda_B} < 1 \quad . \quad (2.18)$$

Chapter 3

Fluorescent proteins

This chapter briefly describes the functioning of fluorescent proteins, both in a more conventional optical and biological view, as well as a laser gain medium. It also describes the properties of the chosen protein, why that specific protein is chosen, and the synthesis process and results.

3.1 Function of fluorescent proteins

The basic function of fluorescent proteins is their ability to absorb and emit photons, with the emitted photons being Stokes shifted (redshifted) in comparison to the absorbed photons [2]. Though the details of the fluorescence mechanisms in fluorescent proteins are complex. Computational studies [8, 9, 10] of the GFP chromophore (which is the optically active part of the protein) shows that the electronic excitation involved in the absorption/emission process is that of a pi-orbital electron that is delocalized in the entire chromophore. Further, the electron being excited is that of the most energetic of the occupied molecular orbitals. The electron is excited to the lowest unoccupied molecular orbital, which is also a pi-orbital delocalized in the entire chromophore. This excitation leads to structural changes

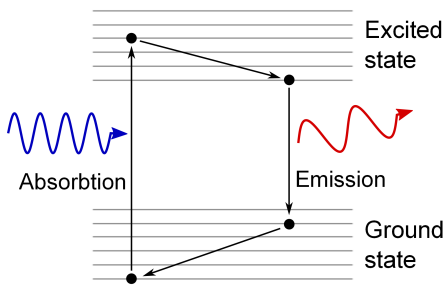

Figure 3.1: Energy diagram model of the fluorescence function in fluorescent proteins.

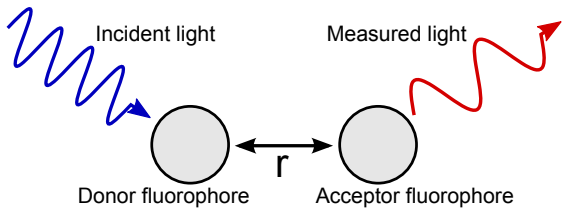

Figure 3.2: Sketch of the FRET concept. A pump photon is incident on the donor fluorophore, which enters a dipole interaction with the acceptor fluorophore which in turn will release the energy through a stokes shifted photon.

in the chromophore, both as a series of chemical reactions as well as changes in the tertiary structure.

The emission process is conceptually very similar. First the excited pi-orbital electron is relaxed back to the state it left earlier, after which the chromophore again will be subject to a series of chemical reactions as well as additional folding changes, which will take the chromophore back to its ground state. An energy diagram of this GFP absorption/emission cycle is sketched in Fig. 3.1, where the chemical and structural changes in the protein are considered sublevels to the electronic excitation.

3.2 The FRET concept

The idea with FRET is, instead of just using one type of fluorophore, to use two different types of fluorophores. Fig. 3.2 shows a sketch of the FRET process, where the first fluorophore, called the donor fluorophore, is optically excited using a laser and can emit light just as it would in a single fluorophore system. The difference is that when a donor fluorophore is "close" ($\lesssim 10$ nm) to a fluorophore of the second kind, called the acceptor fluorophore, the two fluorophores will become dipole coupled and the acceptor fluorophore will emit light instead of the excited donor fluorophore.

The energy transfer efficiency, η, of the dipole coupling relates highly nonlinearly to the distance, r, between the two fluorophores, namely $\eta \propto 1/r^6$ [11]. In biological research this is used to picture and investigate intracellular chemical reactions and how different intracellular components interact. The FRET technique makes it possible to label two different cell components, one with a donor fluorophore and one with an acceptor fluorophore. Imaging this in a fluorescent microscope, it is possible to produce an image that shows where the two cell components are "close" to each other. Analysis of such images can show which different cell components and chemicals interact with each other and in what manner they do it.

3.3 Laser properties of fluorescent proteins

Comparing the energy diagram of GFP (Fig. 3.1) with the energy diagram of the four-level system in Fig. 2.4, the similarities are clear. The most obvious difference is that the GFP protein should be considered a quasi-four-level system rather than a true four-level system, but it is still a possible laser gain material [1]. Even though these simulations are done on GFP, the behavior of other fluorescent proteins should be similar, given that fluorescent proteins are all derivatives of GFP. That is, it should be possible to achieve lasing in other fluorescent proteins as well

Like many other dye gain materials, fluorescent protein based gain materials bleaches in the sense that they are destroyed from being subjected to a too high incident energy, or by going through too many absorb/emit cycles. This is not a new phenomenon amongst dye gain materials, the most common solution to this problem is to have the dye pumped through the cavity, continuously replacing the bleached dye molecules with fresh ones. When working with protein dye lasers this technique might still be used, but with the intention of advancing these lasers to image cells the bleaching problem have to be dealt with in other ways. Using pulsed pump lasers will reduce the incoming mean power and thus the bleaching, while still having peak powers high enough to achieve population inversion.

The excited state lifetimes of fluorophores varies largely with the surrounding environment [12, 13], but typical values in the excited state are a few nanoseconds [1, 12]. Because of this, it could be argued that a suitable pump laser for protein lasers would be pulsed with nanoseconds or shorter pulses in order to achieve lasing during one absorb/emit cycle [1]. However, with longer pulses the initial pulse flank, even if it did not contain enough power to achieve population inversion, would shift the population densities of the different energy levels towards population inversion. It could then be possible to achieve population inversion with a pulse peak power considerably lower than would be required with shorter pulses.

3.4 Venus YFP

The specific fluorophore chosen for this project is Venus YFP. It is chosen for several reasons. YFP is commonly used as acceptor fluorophore in FRET pairs when doing calcium detection [14], and the Venus type of YFP has the advantage of having larger emission cross-section than other types of YFP, which should make it more suitable for lasing. Venus YFP also has a relatively good resistance to changes in acidity and Cl^- concentration [15].

3.4.1 Comparison between GFP and Venus YFP

Since the previously demonstrated fluorescent protein laser employed enhanced Green Fluorescent Protein (eGFP) [1] it is of interest to compare the already used eGFP with the Venus YFP chosen for this project. The first thing to note is that already ordinary enhanced Yellow Fluorescent Protein (eYFP) has a brightness that

is about 1.4 times higher than eGFP at their excitation peaks [16], adding that Venus YFP is about 1.3 times brighter than ordinary eYFP [17] the Venus YFP protein should be easier to achieve lasing with.

The downside of choosing Venus YFP is that, while brighter, it has a fluorescence lifetime that is shorter than GFP [16], and again the Venus build of YFP goes into the more extreme with a fluorescence lifetime that is shorter than ordinary YFP.

3.4.2 Synthesized Venus YFP

The Venus YFP used in this experiment was synthesized using Escherichia coli (E. coli) bacteria. An original stock of already induced bacteria was cultured, after which the monosaccharide L-arabinose was added to a satisfactory concentration in order to trigger the Venus YFP production. The cells were then mixed with glycerol and stored in a freezer. When proteins were needed the stored bacteria were thawed and, using sodium dodecyl sulfate (SDS), the bacteria were opened and the proteins centrifugally filtered. The protocol is described in detail below.

The original stock of induced bacteria were inoculated to a small amount (roughly 3-5 ml) of NZYM broth (a mixture of compounds that stimulates cell growth) together with 100 µg/ml of ampicillin (Amp) and then left to culture over night in a shaker at 37 °C, 200 RPM. After a night of culturing, 0.5 ml of the solution with bacteria was added to 50 ml of NZYM broth with the same concentration of Amp as the culture medium.

This solution was put back into the 37 °C shaker at 200 RPM and left to grow until an absorbance of 0.5 AU/cm at $\lambda = 600$ nm was measured in the solution. At this point L-arabinose was added to a concentration of 0.2% and then put back into the 37 °C, 200 RPM shaker for 4 hours. After this the solution was mixed at a ratio of 1:1 with a 50%/50% mixture of glycerol and distilled water and stored at -70 °C in 2 ml portions.

In order to confirm that the protein generated was in fact Venus YFP, and also because it might be of interest to research lasing from single cells induced with YFP in the future, a sample of bacteria was analyzed using a confocal microscope. A picture of the bacteria can be seen in Fig. 3.3, and a spectrum measured from the bacteria can be seen in Fig. 3.4. The image and the spectrum confirm that the bacteria are producing Venus YFP according to expectations.

When proteins were needed, a sample of stored bacteria was thawed and concentrated prior to performing what is known as lysis. Lysis is basically the breaking apart of cell membranes, used in this application to harvest the Venus YFP synthesized inside the cells. The bacteria were concentrated by centrifuging at 6500 g for 10 minutes and then removing 90% of the storage mixture (thus raising the concentration of bacteria 10 times). The lysis was done with the use of sodium dodecyl sulfate (SDS), which was added to the concentrated bacteria solution to a concentration of 0.03%. Worth noting is that this step was performed with small volumes of concentrated bacteria solution (2 ml) and SDS in low concentration (0.1%), so after this step the total volume of solution was 0.3 ml rather than close

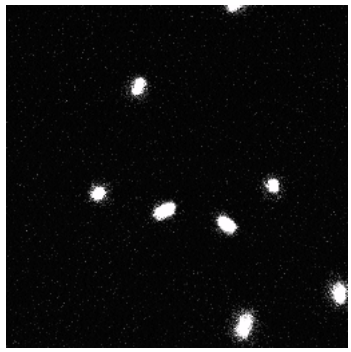

Figure 3.3: Confocal microscope image of thawed Venus YFP producing bacteria prior to lysis, emission at 530 nm. The bright spots are bacteria full of venus YFP.

to the original 0.2 ml remaining per 2 ml portion thawed. After adding SDS, the solution was heated to 50 °C in a water bath for 5 minutes in order to increase the efficiency of the lysis process. The temperature of the solutions was then lowered by placing it on ice for 5 minutes in order not to let the lysis process continue, risking denaturation the Venus YFP protein. Lastly, it was centrifuged at 20000 g for 5 minutes to filter the cell residue from the protein. In Fig. 3.5 images of the YFP generated from this protocol is presented. The images were taken with a

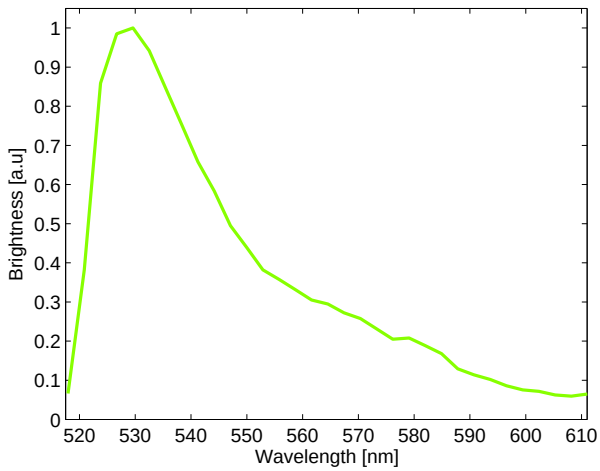

Figure 3.4: Emission spectrum from the Venus YFP, expressed the E. coli bacteria, prior to lysis.

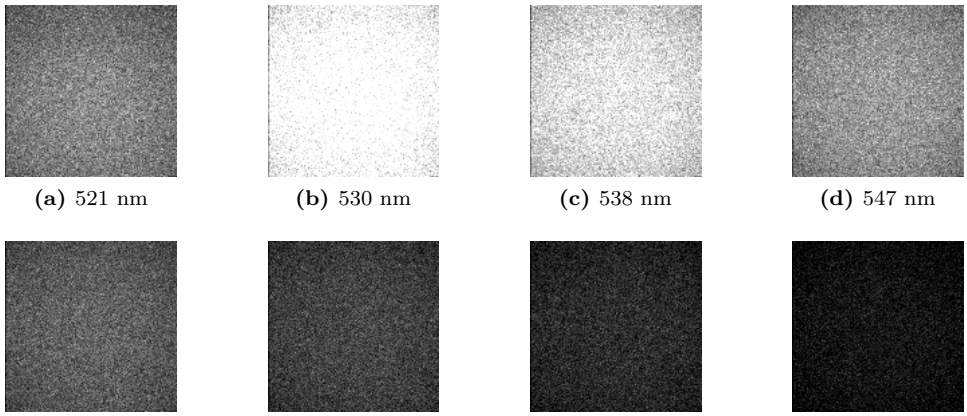

(a) 521 nm **(b)** 530 nm **(c)** 538 nm **(d)** 547 nm

(e) 556 nm **(f)** 565 nm **(g)** 573 nm **(h)** 582 nm

Figure 3.5: Confocal microscope images of the loose YFP protein through lysis with 0.03% SDS. Each image shows different emission wavelengths. The images shows a highly homogeneous solution, and the spectral properties of venus YFP emission is seen when considering the whole series of images.

single sweep of a confocal microscope using 8 simultaneous channels recording one specific wavelength each. Every wavelength is presented in their own image, and across the series the spectral properties of Venus YFP emission is clearly visible. As is clearly distinguishable in the figure, the emission brightest emission of these wavelengths is at 530 nm.

The spectrum of the Venus YFP after lysis had no dramatic changes to it, as seen in Fig. 3.6. The most notable change is the greater susceptibility to Stokes shifting, which is probably caused by the change in environment around the protein after lysis. Stokes shifting being less pronounced in the Venus YFP prior to lysis could prove useful, should experiments with Venus YFP still inside cells be tried. This is because the energy output of the protein is more concentrated to the emission peak of the fluorophore when it is still inside the cells, which is where you would want to have the protein lase.

Alternate sodium dodecyl sulfate concentrations

The above described protocol was not the original protocol. The original protocol for lysis involved an SDS concentration of 0.01% rather than 0.1%. Since this protocol resulted in large debris remaining from the bacteria and even some whole bacteria surviving the process (see Fig. 3.7a), higher concentrations of SDS were tested. At a concentration of 0.02% SDS the amount of debris was drastically reduced, (see Fig. 3.7b), but the solution still was not entirely homogeneous. The greatest concern when adding SDS to higher and higher concentrations was that

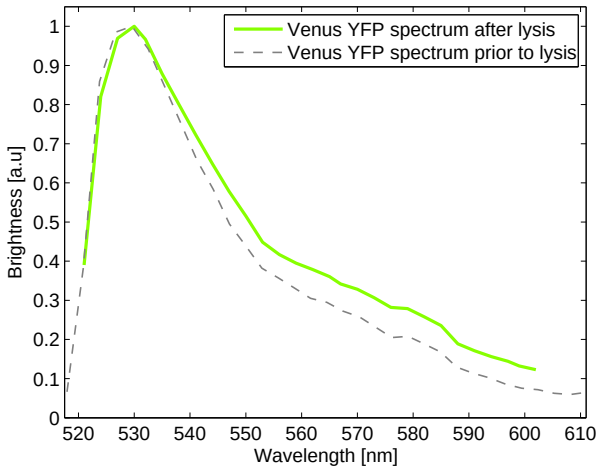

Figure 3.6: Emission spectrum of the Venus YFP after performing lysis. The dashed gray line is the emission from the Venus YFP prior to lysis, the most notable difference being the heightened susceptibility to stokes shift after lysis.

the Venus YFP protein would start to denature, but testing the lysis protocol described in this section revealed that the protein had equal brightness with 0.03% SDS compared to the protein loosened with 0.02% and 0.01% SDS concentration.

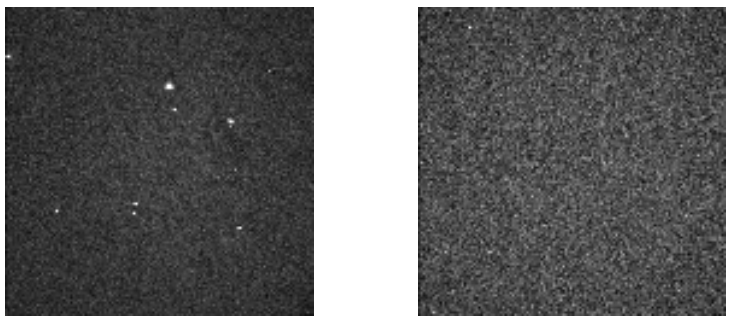

(a) **(b)**

Figure 3.7: Confocal microscope images of the result from lysis protocols with 0.01% SDS (a) and 0.02% (b) SDS, emission at 530 nm. The debris is clearly seen as bright dots in (a), but is not as easily distinguished in (b).

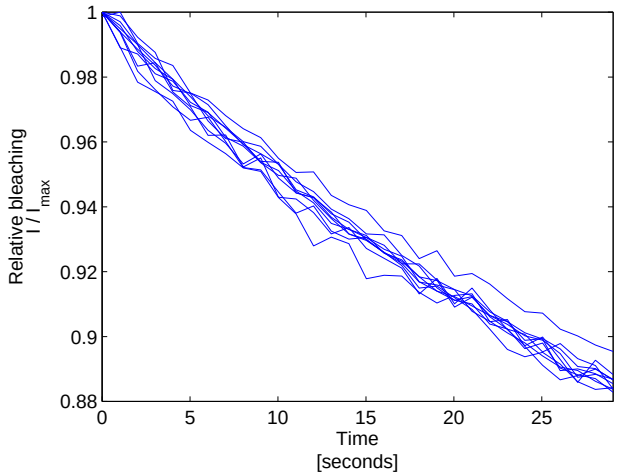

Figure 3.8: Bleaching curves for all 10 channels, with each channel corresponding to one wavelength. As can be seen, there is no sign of any wavelength dependence in the bleaching.

3.4.3 Bleaching properties of Venus YFP

In order to be able to compensate for bleaching during the Venus YFP spectral measurement, a 10-channel measurement (stretching from 521 nm to 599 nm, each channel corresponding to one specific wavelength) with the same exposure time as the highly resolved spectral measurement (shown in Fig. 3.6) was made. The bleaching measurement is limited to 10 channels since this is the maximum number of channels the confocal microscope used can manage in a single sweep. An exponential function is fitted to the data obtained, in turn the fitted function is used to extract the bleaching compensation values. As seen in Fig. 3.8, the bleaching of Venus YFP is not wavelength dependent, at least not during a time interval of about 30 seconds. Since the bleaching is not wavelength dependent, all the bleaching curves are combined to make a data set that the fit was adapted to.

Since every individual fluorophore have a constant and equal probability of being bleached, theory predicts that a good fitting function should be mono-exponential [18]. However, in the case of the Venus YFP that went through lysis using the above described protocol, it seems that a bi-exponential fit is needed to supply a satisfactory fit. The bi-exponential behavior is a sign of two different populations of Venus YFP being present in the protein solution. Similar results have been seen from the enhanced Cyan Fluorescent Protein (eCFP), where two possible conformations of the fluorophore gives raise to two protein populations [19]. The data and the associated fit is displayed in Fig. 3.9. The fitted curve follows the function

$$0.036 \cdot \mathrm{e}^{-0.093t} + 0.964 \cdot \mathrm{e}^{-0.003t} \quad , \tag{3.1}$$

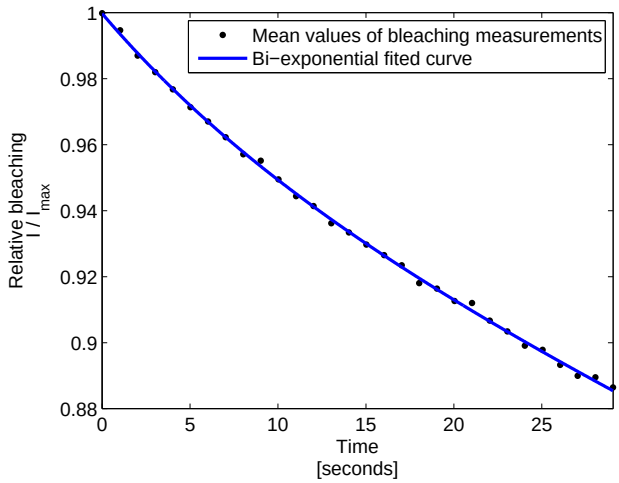

Figure 3.9: Mean value of the 10 channels in the bleaching measurement displayed as black dots with a bi-exponential fit drawn as a blue line.

having residual sum of squares $RSS \approx 2.27 \cdot 10^{-5}$ and a coefficient of determination $R^2 \approx 0.999$. This curve was used to correct for bleaching before plotting the spectrum in Fig. 3.6.

3.4.4 Venus YFP concentration

To determine what concentration of Venus YFP the protocol resulted in, Fluorescence Correlation Spectroscopy (FCS) was used. In FCS the fluorophores in a small confocal volume are used to measure intensity fluctuations over time. The data is then autocorrelated by the function [20]

$$G(\tau) = \frac{\langle \Delta I(t) \Delta I(t+\tau) \rangle}{\langle I(t) \rangle^2} \quad , \tag{3.2}$$

where $\Delta I(t) = I(t) - \langle I(t) \rangle$ and $\Delta I(t+\tau) = I(t+\tau) - \langle I(t+\tau) \rangle$ denotes the deviation from mean photon count at time t and $t + \tau$ respectively. In order to draw any conclusions from the autocorrelated data, a model to describe the fluctuations is needed.

When looking at the light intensity fluctuations in a small volume of solution of a typical fluorescent protein, the two predominant effects are diffusion, making fluorophores enter and exit the measurement volume, and the fluorophores entering and exiting triplet states, making them temporarily bleached. The fact that the number of particles inside the confocal volume at a given time interval is Poisson distributed is used in order to determine the fluorophore concentration in a sample

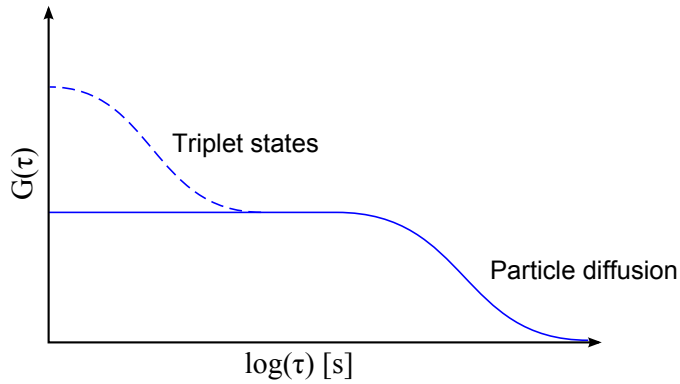

Figure 3.10: Sketch of a theoretical FCS curve. The slower bump is caused by particle diffusing and the higher, dashed, bump is present when the excitation is powerful enough to cause triplet dynamics.

[20]. However, since the entering and exiting of triplet state would alter this distribution, the excitation laser is set to low enough power to cause a negligible amount of triplet states.

To make sure the exciting laser is set to low enough power, one looks at the autocorrelated data. The triplet states have a much faster cycle in an ordinary fluorescent protein than the diffusion (meaning it takes shorter time for the molecule to exit a triplet state once it has entered the triplet state than it takes for a molecule to exit the measurement volume once it has entered the measurement volume). Looking at the theoretical FCS curve in Fig. 3.10, it can be seen that triplet dynamics will show up as an extra, faster, correlation increase on top of the one already present from the diffusion dynamics.

With the Poisson statistics of particle diffusion in mind we start by examining $G(\tau = 0)$. From Eq. 3.2 it is easily seen that

$$G(\tau = 0) = \frac{\langle \Delta I(t) \Delta I(t+0) \rangle}{\langle I(t) \rangle^2} = \frac{\langle \Delta I(t)^2 \rangle}{\langle I(t) \rangle^2} \quad . \tag{3.3}$$

Introducing $I(t) = QN(t)$, where Q is the molecule brightness and $N(t)$ is the number of fluorescent molecules inside the confocal volume at the time t, this becomes

$$G(0) = \frac{\left\langle \left(\Delta QN(t) \right)^2 \right\rangle}{\langle QN(t) \rangle^2} \quad . \tag{3.4}$$

Turning to our definition that $\Delta I(t) = I(t) - \langle I(t) \rangle$ and knowing that $I(t) = QN(t)$, where Q is considered a stationary variable, it is easily realizable that

$$\Delta\big(QN(t)\big) = QN(t) - \big\langle QN(t) \big\rangle = Q\left(N(t) - \big\langle N(t) \big\rangle\right) = Q\Delta N(t) \tag{3.5}$$

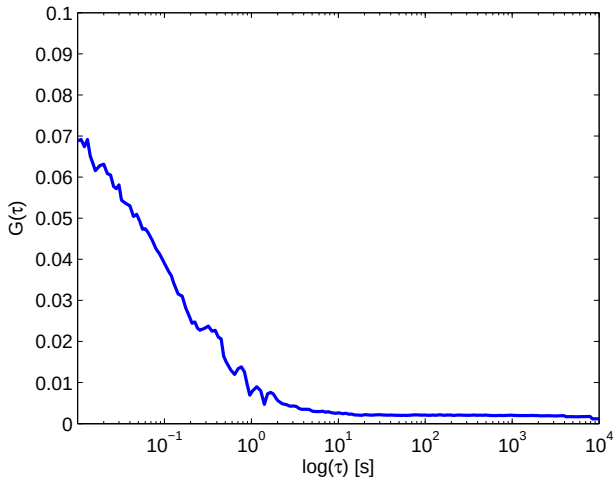

Figure 3.11: Autocorrelation measurement of the YFP solution acquired from the above described protocol.

and so

$$G(0) = \frac{\langle Q^2 \Delta N(t)^2 \rangle}{\langle QN(t) \rangle^2} = \frac{Q^2 \langle \Delta N(t)^2 \rangle}{Q^2 \langle N(t) \rangle^2} \quad . \tag{3.6}$$

Looking closer at the numerator

$$\langle \Delta N(t)^2 \rangle = \left\langle \Big(N(t) - \langle N(t) \rangle \Big)^2 \right\rangle \quad , \tag{3.7}$$

which is the definition of the variance for $N(t)$. As mentioned previously, $N(t)$ is Poisson distributed, which means that the variance is equal to the mean value. Thus

$$G(0) = \frac{Q^2 \langle N(t) \rangle}{Q^2 \langle N(t) \rangle^2} = \frac{1}{\langle N(t) \rangle} = \frac{1}{N} \quad , \tag{3.8}$$

where $\langle N(t) \rangle = N$ is the mean number of fluorescent molecules inside the confocal measurement volume.

With a mean number of particles in the measurement volume known, it is a simple matter to calculate the concentration in the solution. The relation $N = C \mathrm{N_a} V_{\mathrm{con}}$ (where C is the concentration, $\mathrm{N_a}$ is Avogadro's constant and V_{con} is the confocal measurement volume) gives us the final expression

$$C = \frac{1}{G(0) \mathrm{N_a} V_{\mathrm{con}}} \quad . \tag{3.9}$$

The confocal measurement volume in the setup used was calculated to about $V_{\text{con}} = 0.76$ fl using a dye solution of HiLyte 488 with known parameters and using an Olympus dry objective with NA = 1.2 and 60 x magnification. The autocorrelation acquired from the YFP sample is shown in Fig. 3.11, from which $G(\tau = 10^{-2} \approx 0) \approx 0.07$ can be read. These values gives the concentration $C \approx 30$ nM.

Chapter 4

Pulsed 515 nm pump laser

This chapter describes the construction and properties of the solid state laser used to pump the fluorescent proteins.

4.1 Pump laser design

The laser used for pumping the fluorescent proteins was a pulsed solid-state laser, where ytterbium doped potassium yttrium tungstate (Yb:KYW) was employed as the gain medium. It was pumped by a 980 nm laser diode, which was focused into the Yb:KYW. Pulse action was achieved through the technique known as passive Q-switching, using an yttrium aluminum garnet crystal doped with chromium ions (Cr:YAG), placed in Brewster angle, as saturable absorber. The initial transmission of the Cr:YAG crystal was 98%. The laser's output spectra was locked to a wavelength of 1029.3 nm using a VBG with a FWHM bandwidth of 0.32 nm and a peak reflectivity of 99.4%, which was employed as cavity end mirror. The laser beam was extra-cavity frequency doubled using Periodically Poled potassium titanyl phosphate (PPKTP).

The Yb:KYW crystal was a 1.5 mm long, N_g-cut, crystal with a 5% atomic doping of Yb and anti-reflective coating for both the pump and the laser wavelengths at both ends. It was water cooled through a copper holder for thermal stability. A sketch of the 1030 nm laser is shown in Fig. 4.1, a construction with a total length of 25 cm.

To obtain a stable cavity the cavity design needs to fulfill

$$-1 \leq \frac{A+D}{2} \leq 1 \quad , \tag{4.1}$$

where A and D are the respective components from the round-trip ray matrix of the cavity [5]. Ray matrix analysis of the cavity used shows that $\frac{A+D}{2} = 0$. Also, as can be seen from the sketch, the cavity is of W-type, a design that makes it possible to place the Cr:YAG crystal so that it is not bleached by the 980 nm pump.

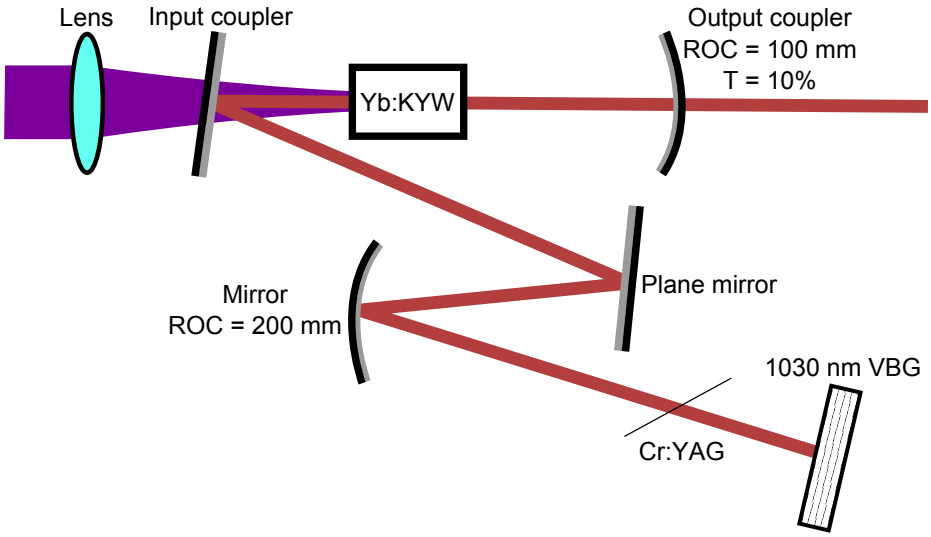

Figure 4.1: Sketch of the 1030 nm pump laser used to generate 515 nm (the frequency doubling setup is not shown).

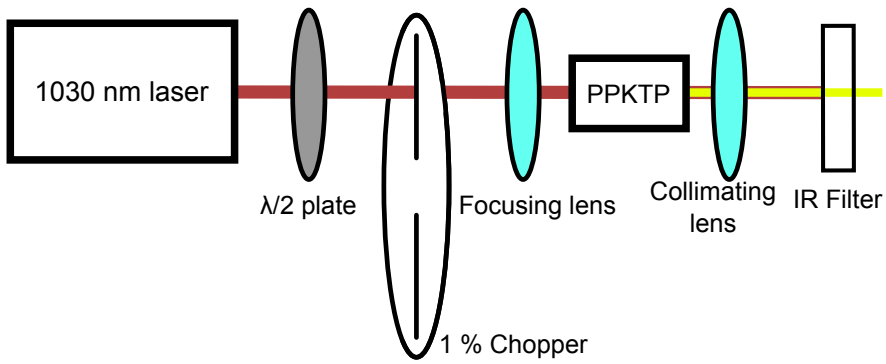

Figure 4.2: Sketch of the frequency doubling of the pump laser, showing the λ/2 plate used to turn the polarization as well as the focusing and collimating lens (100 mm and 30 mm focal length respectively) for the PPKTP used for SHG, and lastly the IR filter to remove the remaining IR light.

Due to the bi-axial property of Yb:KYW, and particularly the different emission cross-sections, the solid-state laser output was polarized. Because of this, a $\lambda/2$ plate was placed directly after the 1030 nm laser, in order to turn the polarization to coincide with the lattice of the PPKTP crystal used to double the frequency. The setup used for frequency doubling is illustrated in Fig. 4.2. The PPKTP had a poling period of 7.99 µm at 82 °C, a temperature that was achieved using a Peltier element. In order to achieve optimal phasematching a 100 mm lens was used to focus the incident beam to a beam waist of approximately 18 µm, which was calculated to be the optimal beam waist according to Boyd-Kleinman theory. The phasematching was further fine-tuned using the crystal temperature as well as the crystal angle in relation to the incident light. Collimation of the output is achieved using a lens with a focal length of 30 mm.

As a last step, the remaining IR light was filtered out using a short pass filter. This in order not to add unnecessary energy to the proteins, that could otherwise cause heating and possibly protein denaturation. The setup also contained a chopper with 1% throughput, used to further limit the total amount of energy that is pumped into the fluorophores, as well as a lens focusing the beam into the PPKTP crystal and a collimating lens after the PPKTP crystal. With the chopper tuned to let through 2 pulses per rotation (one pulse per slit pass), the repetition frequency was lowered by a factor 100 compared to the setup without the chopper in place.

4.1.1 980 nm laser diode properties

The 980 nm pump used to power the 1030 nm solid state laser was a fiber-coupled multiple-emitter diode laser. The fiber had a core diameter of 75 µm and a numerical aperture of 0.22 and the diode had a beam quality parameter, M^2, of about 33. However, it should be noted that the beam quality parameter was determined using the knife-edge technique (as described in Ref. [21]), which gives less reliable results the further from Gaussian the investigated beam is, thus the beam quality parameter of 33 can only be viewed as a general guideline. A 980 nm pump is chosen due to the large absorption cross-section, for polarization in the N_m axis direction, around 980 nm in Yb:KYW. The absorption cross-section of Yb:KYW is shown in Figs. 4.3 a) and b) [22].

The diode had a polarized output, though after passing the fiber the polarization was not preserved. The maximum power difference after the fiber of two perpendicular polarization directions was 5%. As for output power, a plot of the output power in relation to the drive current is presented in Fig. 4.4 [21]. The threshold current is about 0.8 A and it has a slope efficiency of about 0.5 W/A. During the measurement the diode temperature was held at 18 °C.

Further, the output spectrum of the 980 nm laser diode is tunable by both temperature and drive current. This is illustrated by the measurement displayed in Fig. 4.5, where an optical spectrum analyzer (OSA) with a resolution of 0.07 nm was used to measure the spectrum of the 980 nm laser diode at two temperatures and different drive currents [21]. In order not to damage the OSA, the beam was

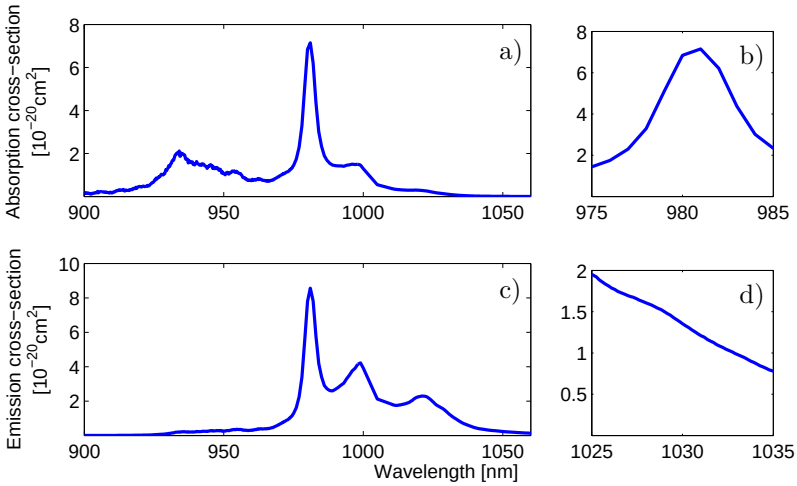

Figure 4.3: Cross-sections of Yb:KYW for polarization along the N_m axis [22]. a) and b) are absorption cross-sections, with b) being zoomed in at the area around 980 nm. c) and d) are emission cross-sections, with d) being zoomed in at the area around 1030 nm.

attenuated prior to measuring the spectrum, and, since the diode laser is of a multi-emitter construction, the emitted beam is focused into a multi-mode fiber coupled to the OSA. With no focusing, the spectrum of the beam varies with position inside the beam.

4.1.2 Solid state laser properties

The properties of the 1030 nm solid state laser was established, both using the VBG for wavelength-locking as described above, as well as employing a highly reflecting dielectric mirror employed as cavity end mirror.

Both setups had a polarization ratio of 1:100, with the polarization oriented along the N_m axis of the crystal. The polarized output is due to the N_m axis having a significantly larger cross-section than any of the other axes in Yb:KYW. The emission cross-section for the N_m axis in Yb:KYW is shown in Figs. 4.3 c) and d) [22].

Wavelength locked Yb:KYW solid state laser

Using the VBG as a cavity end mirror, the threshold power for the pulsed 1030 nm laser was around 17.5 W. However, when pumping at low powers, the pulsed action of the laser was highly irregular, with pulse peak power varying randomly between 400 mW and 1.6 W, and repetition rate varying between 4 kHz and 8 kHz. At pump

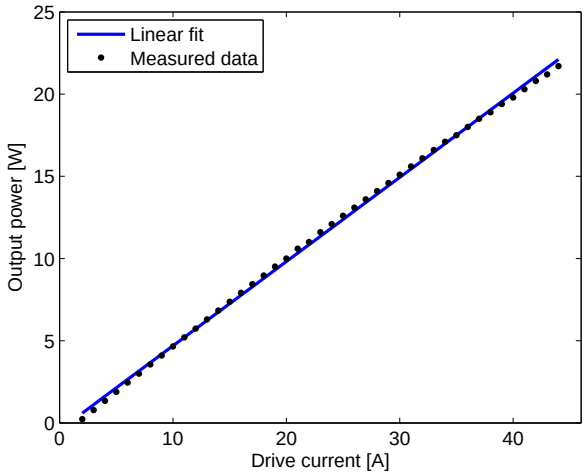

Figure 4.4: 980 nm optical power output plotted against the diode current for the 980 nm laser diode pump. The threshold current was about 0.8 A, with a slope efficiency of about 0.5 W/A [21].

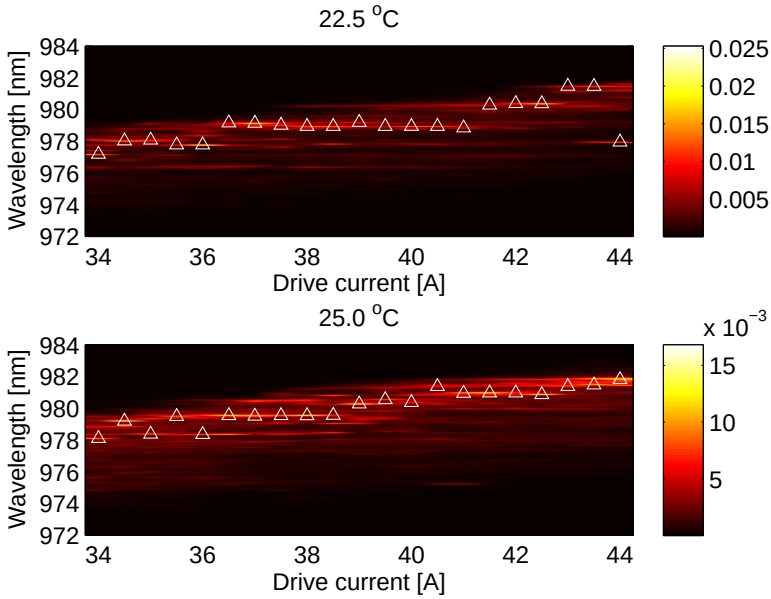

Figure 4.5: 980 nm laser diode relative powers at different wavelengths for two different temperatures. Triangles marks peaks.

powers of 18W, the pulse action stabilized and it was possible to measure the pulse properties. The measured power and repetition rate characteristics are shown in Figs. 4.6 and 4.7, with pulse durations between 250 ns and 270 ns FWHM.

Fig. 4.6 shows the power dependencies, both average powers with and without pulsed action as well as the pulse peak powers when having pulsed action, while Fig. 4.7 shows the repetition rate as a function of input power. The error bars in the plots are measured standard deviations for the peak power and repetition frequency, respectively. All measurements were done using a photo diode with a rise time of 1 ns, and, in order not to damage or saturate the photo diode, the light was reflected off a glass surface prior to being incident on the diode.

When having the pulsed action of the laser engaged the slope efficiency was about 0.52 in the region where the pulsed action was unstable, and about 0.11 in the region where it was stable, a difference that is easy to see in Fig. 4.6. In the analyzed region, the average output power rises from about 400 mW to about 950 mW. The setup without having the pulsed action engaged have an average output between about 750 mW and 1350 mW, with a continuous slope efficiency of around 0.21. The higher average power of the CW laser action is expected, since the Q-switching pulsing technique introduces an additional cavity loss.

The reason for the pulse instabilities at lower pump powers, as well as the more rapidly rising average output power, is that when having a pump that is almost sufficient to achieve enough gain to compensate for the cavity losses (including the saturable absorber), random fluctuations in the light intensity will cause the gain to momentarily be enough to compensate for the cavity losses, thus achieving lasing. This lasing will pump the saturable absorber, so that the absorption is lowered, at which point the average gain level is enough to continue the lasing and the saturable absorber will become fully saturated. When the pump power is enough to have a stable pulse action, both the average output and pulse peak power steadily rises.

As for the repetition rate (Fig. 4.7), it shows no apparent correlation to changing the incident pump power, but lies between 8 kHz and 9 kHz, with a standard deviation of about 200 Hz.

The beam quality parameter of the wavelength-locked 1030 nm solid state laser was measured using the knife edge technique, employing a 200 mm focusing lens. Results from the measurement and an associated fit can be seen in Fig. 4.8, a results which shows that M^2 is close to 1.

The spectral properties of the wavelength-locked solid-state laser can be seen in Fig. 4.9. The two visible peaks are located at 1029.56 nm and 1029.74 nm respectively, and the whole spectrum has $\Delta\lambda_{\mathrm{FWHM}} \approx 0.8$ nm. The large measured bandwidth in comparison with the bandwidth of the VBG is due to the use of a multi-mode fiber to couple the beam into the OSA, which gives rise to several incident angles for the light on the OSA prism.

As for longitudinal modes, the mode spacing is

$$\Delta\nu = \frac{\mathrm{c}}{2L} \quad , \tag{4.2}$$

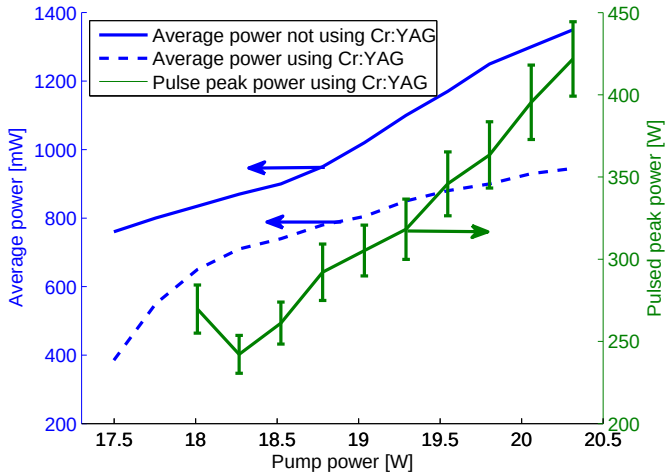

Figure 4.6: Power characteristics of the solid state laser when locked to 1030 nm using the VBG. Both average powers with and without pulsed action, as well as pulsed action peak powers, are shown in the figure. The error bars on the pulse peak power plot shows the measured standard deviation of the pulse peak.

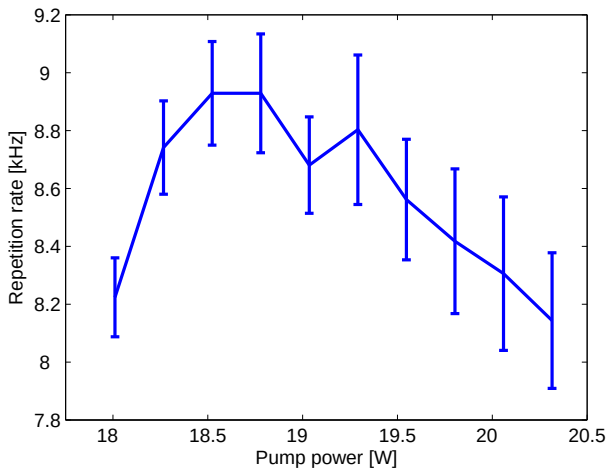

Figure 4.7: Repetition rate characteristics of the solid state laser when locked to 1030 nm using the VBG. The error bars shows the measured standard deviation of the repetition rate.

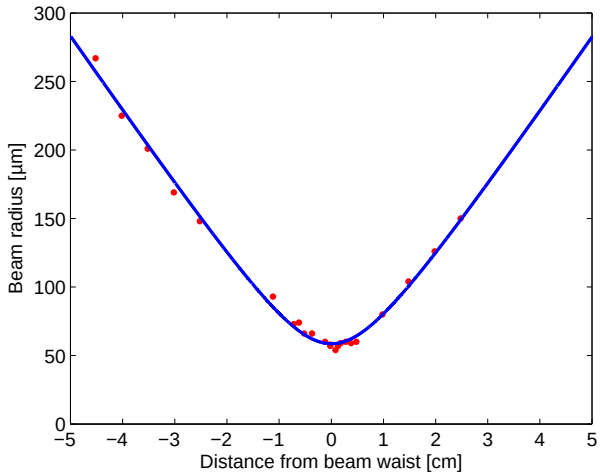

Figure 4.8: Wavelength-locked 1030 nm laser beam quality measurement. The beam quality factor was determined to be close to one, with a pump power of 18 W. The red dots are the measurement results and the blue line is the associated fit.

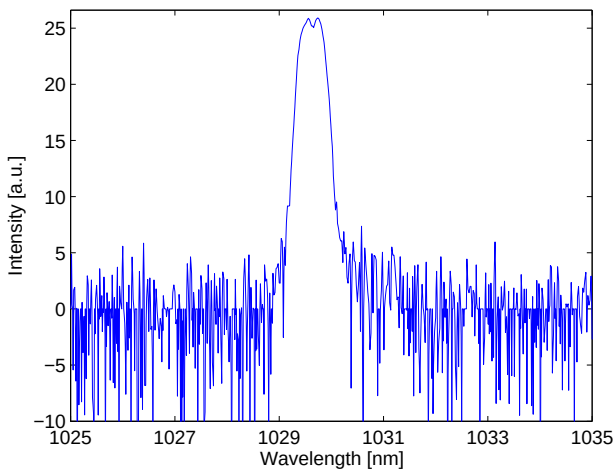

Figure 4.9: Output spectrum of the wavelength-locked 1030 nm solid state laser. The two peaks are located at 1029.56 nm and 1029.74 nm respectively, $\Delta\lambda_{\mathrm{FWHM}} \approx 0.8$ nm. The large bandwidth in comparison with the bandwidth of the VBG is due to the use of a multi-mode fiber to couple the beam into the OSA, which gives rise to several incident angles for the light on the OSA prism.

where c is the speed of light and L is the optical length of the cavity. In terms of wavelength, the equation becomes

$$\Delta\lambda = \frac{\lambda^2}{2L} \quad , \tag{4.3}$$

which, with $L = 251.5$ mm, becomes $\Delta\lambda \approx 2$ pm. Using the measured zero-to-zero spectral width of about 1.4 nm, the number of longitudinal modes would be about 650. Though considering the spectral broadening in the measurement due to the use of a multi-mode fiber it is possible that the actual $\Delta\lambda$ is closer to 0.32 nm, in which case the number of longitudinal modes would rather be about 150.

Yb:KYW solid state laser with no wavelength locking

The solid state laser characteristics when employing a flat, highly reflecting mirror (R > 99.9%) as cavity end mirror instead of the VBG, are shown in Fig. 4.10 and Fig. 4.11. Fig. 4.10 shows the power characteristics, and Fig. 4.11 shows the repetition rate of the laser. With this setup, the pulsed action was stable at low 980 nm pump powers, though over input pump powers of ∼19.4 W both the repetition rate and peak powers started varying in such an unstable and rapidly fashion that characterization was not possible with the available equipment. Simultaneously as the pulsed action became unstable the average output power increased drastically, taking a sudden step from 380 mW to 570 mW of output power when increasing the pump power from 19.3 to 19.5 W. The jump in output power when entering the unstable region of lasing corresponds to a slope efficiency of 0.73, which, in comparison to the slope efficiency for the rest of the curve at about 0.10, is very large. The repetition rate of the non wavelength-locked Yb:KYW solid state laser raised steadily from 7.5 kHz to 12.5 kHz with standard deviations around 500 Hz as the pump power was increased, until the breakdown at about 19.4 W. The FWHM pulse durations was between 410 ns and 490 ns.

The reason for having stable pulse action at low powers, where the wavelength-locked setup was unstable, is that the highly reflecting mirror is less lossy than the VBG. With a slightly lower round-trip loss, the overall gain of the system rises, effectively having the same effect as increasing the pump power from a cavity gain/loss perspective. That is, the threshold pump power for the instabilities is lowered, and so it is possible to have a stable pulse action with lower pump powers.

The cause of the breakdown at higher pump powers is unknown, and in order to draw any clear conclusions further studies that are outside the scope of this project would be needed. However, analysis of the spectral properties of the pulsed setup without wavelength-locking suggests that the unstable nature of the setup could be related to the laser rapidly changing between lasing modes. Three different lasing states were identified in the analyzed region, as is seen in Fig. 4.12. During low pump powers the spectrum was stable at the spectral range shown in the uppermost plot in Fig. 4.12, which is centered around 1043.6 nm with $\Delta\lambda_{\mathrm{FWHM}} \approx 1$ nm. When increasing the pump power to about 18.8 W, the state of the laser changes, and

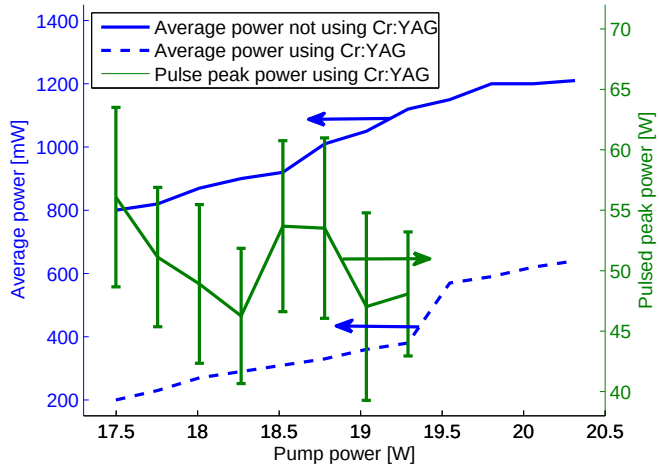

Figure 4.10: Power characteristics of the Yb:KYW solid state laser without wavelength locking. The pulsed action of the laser was steady until a pump power of about 19.4 W, at which point the pulse action broke down to a highly unstable state. At the same point, the average power of the laser increased drastically. The error bars show measured standard deviation error.

the frequency is slightly increased. In this second state the spectrum is centered at 1040.6 nm, though still having $\Delta\lambda_{\mathrm{FWHM}} \approx 1$ nm. In this second spectral range, the spectrum of the laser was slightly less stable, occasionally changing to the highest frequency state (which can be seen in the lowest plot).

With further increase of pump power the spectral instability increased. At a pump power of about 19.8 W the spectral range entered a state where it fluctuated randomly back and forth between the two wavelength bands that can be seen in the lowest plot. However, the wavelengths bands weren't entirely stable, both with regards to their center wavelength as well as their bandwidth. Roughly their center wavelengths was within 1036 nm to 1038 nm and 1040 to 1042 nm respectively, with a FWHM bandwidth of about 0.5 nm to 1.5 nm. This behavior shows the necessity of wavelength locking for Yb:KYW lasers.

Using Eq. 4.3, the number of longitudinal modes for the two stable modes of this setup can be calculated as well. The stable states has $\Delta\lambda \approx 1.5$ nm, with a negligible difference in center frequency. Eq. 4.3 then shows that they both have about 700 longitudinal modes.

4.1.3 515 nm frequency doubled output

The frequency doubled output of 515 nm coincides very well with the absorption peak of YFP [23]. The use of Venus YFP should have little to no effect of the

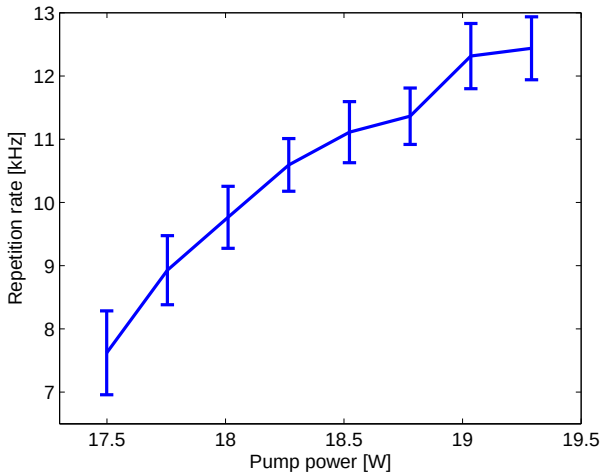

Figure 4.11: Repetition rate of the Yb:KYW solid state laser without wavelength locking. The repetition rate raised steadily to 12.5 kHz, at which point the input pump power was 19.3 W. With further increase of the pump power the pulse action entered a highly unstable state. The error bars show measured standard deviation.

pump efficiency, due to the absorption spectrum being very similar to ordinary YFP [15]. The OSA used to measure the 515 nm output had a resolution of 10 pm, the spectrum can be seen in Fig. 4.13 and is centered around 514.85 nm with $\Delta\lambda_{\mathrm{FWHM}} = 0.1$ nm.

When having the polarization optimized to the c-axis of the PPKTP crystal to exploit the d_{33} coefficient, and the 1030 nm pump was driven at the highest possible power without damaging the PPKTP crystal, the average power, without the chopper activated, was about 100 mW in the 515 nm regime. A measurement of the Second Harmonic Generation (SHG) is shown in Fig. 4.14, it was about 18%, with no apparent dependence with the input power. Theoretically, the SHG output power from phase-matched SHG varies quadratically with the pump power [24]

$$P_{\mathrm{SHG}} \propto P_{\mathrm{pump}}^2 \quad . \tag{4.4}$$

The linear behavior seen in this setup is probably related to green induced IR absorption. With higher pump powers more 515 nm light will be generated, increasing the absorption of the 1030 nm light in the crystal. The increase of 1030 nm absorption is enough to cause a linear dependence between the input pump power and SHG output power.

Since it is desirable to have as much freedom as possible to choose output power while still maintaining stable pulse characteristics, the 1030 nm laser was constantly

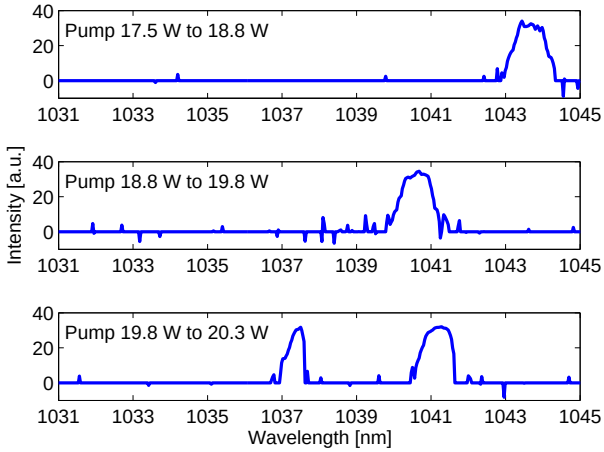

Figure 4.12: The three spectral ranges of the Yb:KYW solid state laser without wavelength-locking. The uppermost plot shows the spectral mode for low pump powers, the middle plot shows the intermediate mode and the lowest plot shows the two modes that the laser rapidly oscillates between at high pump power.

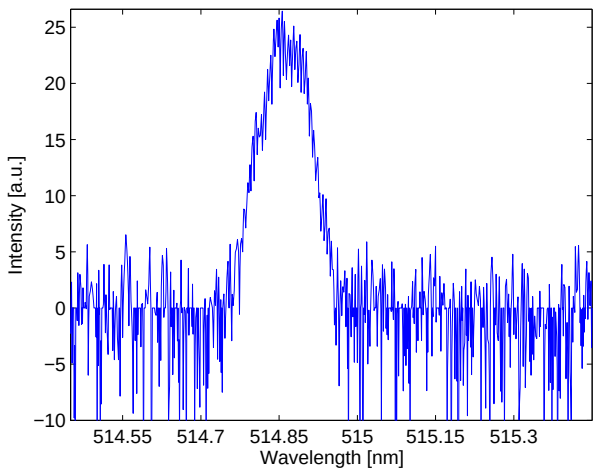

Figure 4.13: Output spectrum after frequency doubling the wavelength-locked 1030 nm laser to 515 nm. The spectrum is centered around 514.85 nm with $\Delta\lambda_{\mathrm{FWHM}} \approx 0.1$ nm.

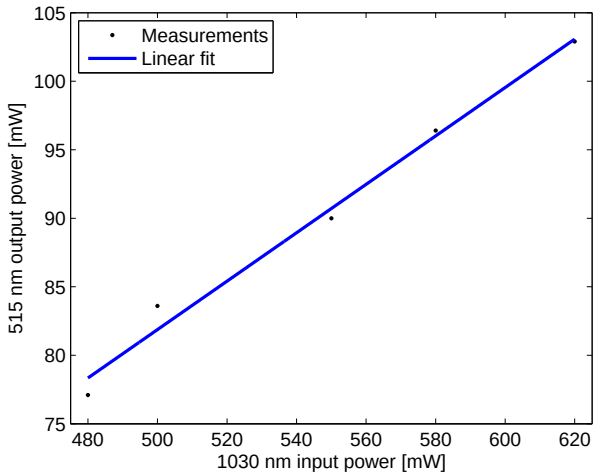

Figure 4.14: Results from a measurement of the SHG efficiency, the efficiency is about 18%. Having a linear rather than quadratic characteristic is probably due to green induced IR absorption.

driven at its maximum output power with regards to not damaging the PPKTP crystal. Attenuation of the 515 nm output was achieved by rotating the $\lambda/2$ plate placed prior to the frequency doubling PPKTP crystal, thus altering the portion of light having a polarization corresponding to the KTP crystal lattice in the PPKTP crystal. The repetition frequency at the maximum possible 515 nm output was 8.6 kHz, which translates to a repetition rate of 86 Hz in the 515 nm regime with the chopper activated.

4.2 KTP damage threshold

KTP is a popular material to use when doing periodically poled quasi-phase-matched frequency doubling to the visible regime. This is because of the high damage threshold of KTP, which is usually quoted as around 1 GW/cm^2 at 1064 nm with 10 ns pulses at 10 Hz. However, during the construction of the pump laser it was found that permanent damages appeared in the KTP crystal already at power densities of 33 MW/cm^2.

Since an attenuator was used to control the pump output power, the SHG was optimized in order to give as much freedom as possible when choosing different output powers. The optimization was done using Boyd-Kleinman theory using the analytical function suggested by Chen and Chen [25], which estimated the optimal focus to 18 µm.

In order to achieve this focus inside the KTP crystal, the known physical ge-

ometry of the 1030 nm laser was used, assuming $M^2 = 1$, to simulate the beam focusing using ray-tracing software. It was found that a focusing lens of 100 mm positioned 115 mm from the crystal would give a focus inside the PPKTP crystal of about 18 µm.

Using this setup, permanent damage to the PPKTP crystal was observed already at laser mean powers of 0.58 W, which translates to pulse peak powers of about 340 W. With a beam waist of 18 µm this corresponds to a damage threshold of about 33 MW/cm^2, well under the usually quoted 1 GW/cm^2 at 1064 nm with 10 ns pulses at 10 Hz. Pictures of the damages can be seen in the images displayed in Fig. 4.15.

It has been suggested that this phenomenon of greatly reduced damage threshold for PPKTP when doing SHG of semi long pulses is related to green-induced gray-tracking in the KTP [26, 27]. Because of this, the same setup was tried with a Periodically Polarized Rubidium doped potassium titanyl phosphate (PP-RKTP), which is less prone to gray-track than ordinary PPKTP [28]. However, the PP-RKTP experienced permanent damaging already at peak power densities of about 24 MW/cm^2, a result that suggests that the phenomenon causing this permanent damage is not related to green-induced gray-tracking.

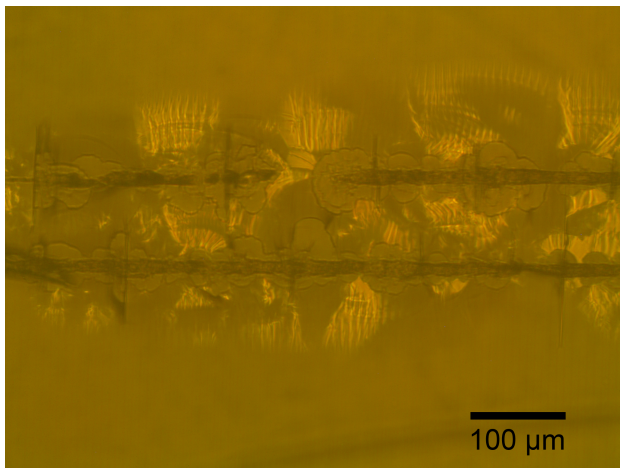

(a) KTP damage seen perpendicular to the optical axis. The second path is probably due to the crystal damage spreading along the surface reflection from the short pass filter.

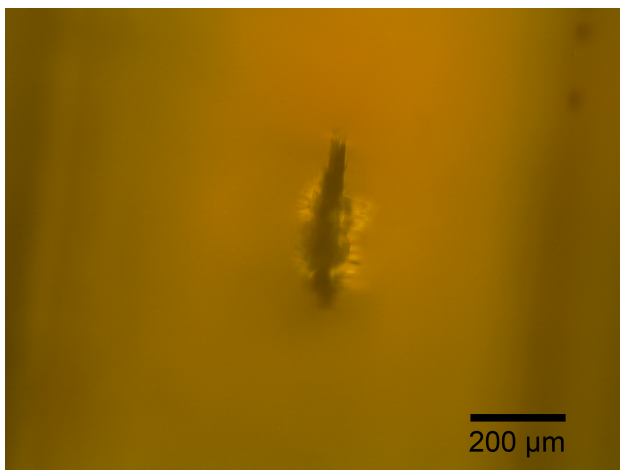

(b) KTP damage seen from top of the crystal. The sides of the crystal can be slightly distinguished at the left and right.

Figure 4.15: The damages obtained in the KTP crystal.

Chapter 5

YFP laser

This chapter describes the design and function of the YFP dye laser.

5.1 YFP laser cavity design

As previously mentioned, one great possibility of biological lasers is to have FRET lasing in order to circumvent the low signal values that is otherwise characteristic for FRET applications. To achieve FRET lasing, one would want to have the acceptor fluorophore lasing while suppressing lasing from the donor fluorophore. Lasing from the donor fluorophore would most likely bleach the donor fluorophore faster than otherwise, and it could also contribute to high intensity leakage into the signal wavelengths.

Most fluorophores have a relatively broad emission spectrum, and more so than others the common donor fluorophores Blue Fluorescent Protein (BFP) and Cyan Fluorescent Protein (CFP) [23]. Because of this, in order to suppress lasing from the donor fluorophore and still have sufficient reflectivity to be able to have lasing from the acceptor fluorophore, it is desirable to have a cavity containing mirrors with very narrow reflectivity bandwidth, or at least a very sharp reflectivity cut-off. To manufacture dichroic mirrors that have these properties is very expensive and complex, and sometimes it is not even possible with todays commercially available manufacturing techniques.

A cheaper, and possible, solution is to use a VBG. VBGs have a very narrow bandwidth (< 0.1 nm FWHM), and are possible to manufacture with relatively high ($>99\%$) reflectivity [29]. It is also possible to tune the wavelength a VBG reflects by adjusting the incidence angle and by altering the grating temperature. Thus, with a cavity containing at least one VBG, it would be possible to use the same cavity to lase many different fluorophores, as long as the other mirrors in the cavity have high reflection at the emission wavelength of the fluorophore.

A sketch of the Venus YFP laser design can be seen in Fig. 5.1. Note that the cavity is folded into three dimensions. This is because the Venus YFP solution is

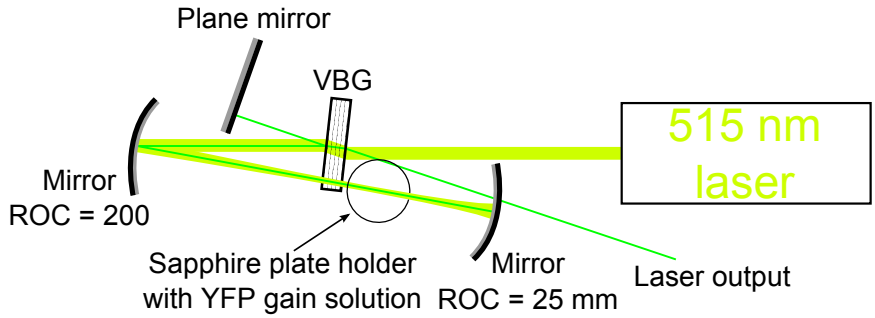

(a) Protein laser design as seen from top.

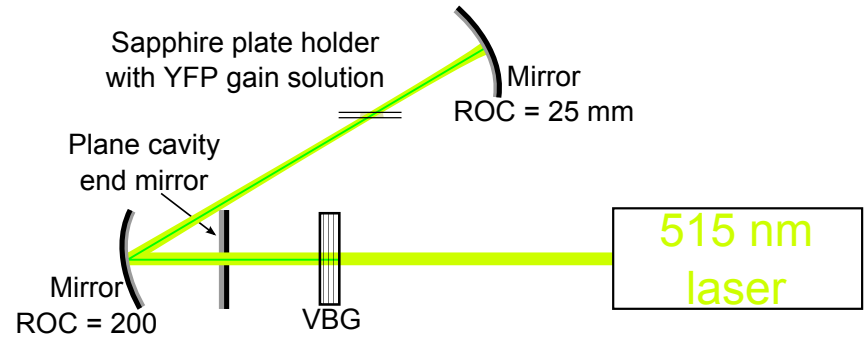

(b) Protein laser design as seen from the side.

Figure 5.1: A schematic sketch of the protein laser design. The top image is the design as seen from the top and the bottom image as it is seen from the side. Note that the cavity is folded into three dimensions. In order too make the sketch more clear the laser output has been omitted in the bottom image.

held between two sapphire plates, which, in order to cause minimal surface reflection losses, are mounted in Brewster angle with respect to an interface with air. With a refractive index of about 1.77, the Brewster angle in an air-sapphire interface is around 60.5°.

To prevent the protein solution from pouring out of the container the sapphire plates needs to be kept horizontal, so to get an incidence Brewster angle with horizontally placed sapphire plates the cavity itself is angled upwards. Since the mirror folding the cavity is curved, the beam is directed over the VBG in order to minimize the astigmatism that is introduced from having a non zero incidence angle on curved mirrors. Thus the sapphire plates and the curved cavity end mirror are situated higher off the optical table than the other components.

Since the VBG will have virtually no reflectance of the pump laser and a reflectivity of just above 99% for the lasing wavelength it is used as both input and output coupler. The pump laser is then reflected off the curved folding mirror

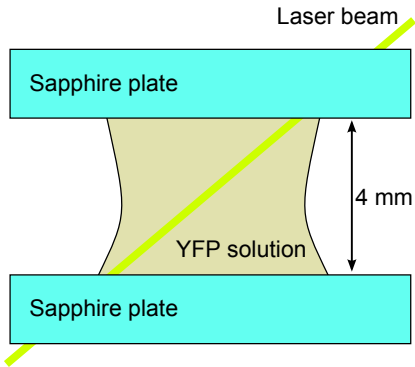

Figure 5.2: A sketch of the sapphire plate holder constructed to hold the protein solution gain material.

(ROC = 200 mm) and passed through the protein solution container, after which the cavity is closed using the curved cavity end mirror (ROC = 25 mm). Since the VBG is angularly tuned to match the emission peak of Venus YFP, a plane mirror is used to close the cavity at the other end. The total length of the cavity is about 22 cm.

The sapphire plates making the protein solution container are separated by 4 mm, in between which the protein solution is kept during the experiment, as is sketched in Fig. 5.2. Sapphire is chosen because of its heat conducting properties in combination with having excellent optical properties. The fact that the beam is passed through the sapphire plates in Brewster angle will also affect the length the laser travels through the gain medium. The incident angle of 60.5° makes the distance the beam actually travels through the protein gain medium about 4.6 mm.

Even though the VBG have an extremely narrow reflective bandwidth there are surface reflections from the pump off the VBG. Since the lasing from the proteins is expected to be very weak, even a surface reflection from the pump could be a problem when trying to detect the signal. What is not shown in Fig. 5.1 is that the pump surface reflection from the VBG along with the supposed signal is separated by having them incident on a reflecting grating and separating them by wavelength before having the supposed signal aimed at a detector.

5.1.1 VBG limitations

As mentioned, the properties of VBGs make their reflectance properties sensitive to incidence angle as well as beam angular divergence. Thus, a light source that is too highly focused will not be efficiently reflected using a VBG. Eq. 2.18 shows an expression for when a plane wave approximation of the light incident on the VBG is applicable, that is, when the VBG will act as an efficient mirror.

The VBG used in the cavity has a bulk refractive index of $n_0 = 1.49$, peak reflectivity (for normal incidence) at $\lambda_B = 533.2$ nm and a FWHM bandwidth $\Delta\lambda_{\mathrm{FWHM}} = 0.4$ nm. The grating can be considered a strong grating, so the approximation $\Delta\lambda_{\mathrm{FWHM}} \approx \Delta\lambda$ is valid. The light incident on the VBG has a wavelength of $\lambda_R = 530$ nm and simulating the cavity using ray-tracing software gives the collimated beam width $\omega_{e^{-2}} = 450$ µm.

Putting all this into Eq. 2.18 it is clear that the plane wave approximation is fulfilled with a good margin for this cavity:

$$\frac{\pi}{4} n_0 \frac{\omega_{e^{-2}}}{\lambda_B^2} \Delta\lambda \approx 0.74 > \sqrt{1 - \left(\frac{\lambda_R}{\lambda_B}\right)^2} \approx 0.11 \quad . \tag{5.1}$$

5.1.2 VBG alignment in cavity with limited gain material lifetime

Because of the very narrow reflectivity of VBGs, aligning cavities containing one or more of them can be difficult and take a long time. Since the fluorescent proteins used as gain medium in biological lasers has a limited fluorescence lifetime due to bleaching, it would be very convenient if the cavity could be aligned already before the gain medium is placed in the cavity.

To attend to this problem a fiber laser emitting at 1060 nm was constructed and frequency doubled using a lithium triborate (LBO) crystal. The 530 nm beam was then aligned to coincide exactly with the 515 nm beam from the pump laser (Fig. 5.3a). The VBG was inserted into this configuration and aligned to reflect the 530 nm beam, this will cause a slight translation of the 515 nm beam when it passes through the VBG (Fig. 5.3b). Theoretically it should now be sufficient to make sure that the 530 nm beam is retro-reflected off the cavity end mirror in order to have an aligned cavity. However, to make sure that the 515 nm beam is incident on a spot where there is poling present in the glass, the 530 nm beam was realigned to match up with the 515 nm beam again and then adjusted to retro reflect off the cavity end mirror (Figs. 5.3c and 5.3d). After these steps, the pump laser is simply used to align the rest of the cavity. Of course the cavity end mirror could be replaced with a more complex system for retro-reflection, should the VBG be located in the middle of a more complex cavity.

5.2 YFP laser function

Lasing was not achieved with the above described setup. Several possible reasons why lasing was not achieved have been identified, where the most probable reason is that the gain is too low as a result of a too low protein concentration and a too poor protein purity. A more elaborate discussion concerning this problem can be found in Sec. 5.2.1.

Another side of the same coin, but something still worth mentioning, is that the cavity described above is relatively lossy, with a round trip loss of about 2.5%.

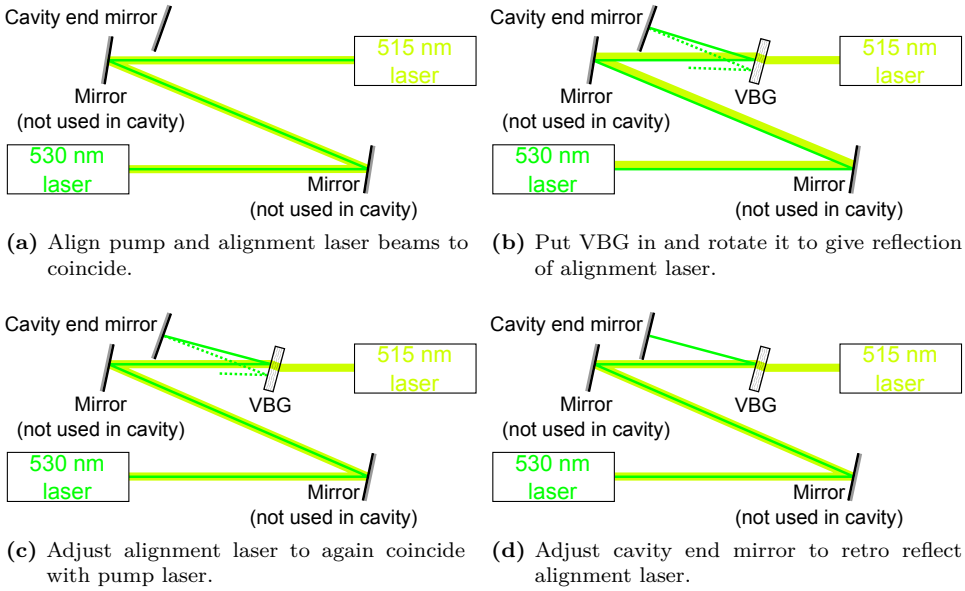

(a) Align pump and alignment laser beams to coincide.

(b) Put VBG in and rotate it to give reflection of alignment laser.

(c) Adjust alignment laser to again coincide with pump laser.

(d) Adjust cavity end mirror to retro reflect alignment laser.

Figure 5.3: Scheme of the method used to align the VBG correctly prior to adding the gain medium into the cavity.

The cavity used for previously demonstrating protein lasing is constructed of two mirrors that are highly reflecting at the emission wavelength of the protein [1], which accounts for an extremely low loss cavity (round trip loss $< 0.2\%$). A four mirror cavity, where one of the mirrors is a VBG, could never come close to the low loss of the simple cavity used for the first demonstration.

A third possibility is that the proteins are destroyed before population inversion can be achieved. Speculating in the exact fluorescence lifetime of the Venus YFP molecules is hard, since the fluorescence lifetime is very dependent on the surrounding environment. However, with a 22 cm long cavity, the round-trip time is about 1.5 ns, and given that the bleaching measurements showed fluorescence over several seconds even at high energy CW pumping (which indicates a good environment for the fluorophores) it is safe to say that the YFP molecules should be able to emit light long enough to achieve population inversion. Of course, if the pulse from the pump is long enough to have the proteins absorb enough power to denature before the critical pump power can be reached, the proteins will not lase. This problem would require a redesign of the pump laser in order to make the pump pulse shorter, reaching threshold energy without having the fluorophores being subject to a long period of incident energy that is not enough to get population inversion amongst the proteins.

5.2.1 Venus YFP concentration and purity

The previously demonstrated GFP lasing had an optimal lasing threshold at concentrations between 10 μM and 100 μM, with a rapid increase of power needed to reach lasing threshold when having lower or higher concentrations [1]. With a measured Venus YFP concentration 3 orders of magnitude lower, it is likely that it is impossible to achieve lasing with the Venus YFP synthesized from the process developed for local synthesis. On top of the significantly lower protein concentration there is also the fact that the cavity designed for this experiment is lossier than the cavity used to demonstrate GFP lasing. Light transmission measurements also show signs of poor pump laser absorption in the gain medium, as low as 0.013 cm^{-1}. This was measured using an UV-VIS spectrophotometer (Hitachi U-1900), with a zero reference sample consisting of a solution produced with cells that had not been cultured using L-arabinose, but otherwise had been subject to the same protocol as the Venus solution.

It might be possible to deal with the low gain by increasing the length of the gain medium, but since this gain medium is dissolved in water, a long gain medium length would also introduce increased scattering off the water molecules. Moreover, the measured absorption of 0.013 cm^{-1} is too high for the, by FCS, measured concentration. Venus YFP has an extinction coefficient of $92.2 \cdot 10^3$ $\text{M}^{-1}\text{cm}^{-1}$ [15], an absorption of 0.013 cm^{-1} corresponds to a concentration of

$$\frac{0.013 \text{ cm}^{-1}}{92.2 \cdot 10^3 \text{ cm}^{-1}} \text{ M} \approx 1.4 \cdot 10^{-7} \text{ M} = 140 \text{ nM} \quad . \tag{5.2}$$

This suggests that most of the energy that is absorbed in the solution is not absorbed in the Venus YFP, but in other components of the solution. Most likely these parasitic absorbers are cell residue left from the lysis process which are too small to separate using centrifuging techniques.

Chapter 6

Discussion and outlook

This chapter concludes what has been done during the scope of this project and discusses possible ways to progress in the field of biological dye and FRET lasers.

6.1 Conclusions

Venus YFP proteins were synthesized locally using a fairly simple, although well established, method. The final Venus YFP solution concentration was measured by FCS to about 30 nM, but absorption measurements showed signs of much debris still being present in the solution, absorbing much of the pump light. The emission spectrum of the synthesized Venus YFP was measured in order to be able to fine tune the laser construction.

Further, a linearly polarized passively Q-switched 1030 nm Yb:KYW laser was constructed for pumping. A $\lambda/2$ plate was used to attenuate the laser and KTP utilized to achieve frequency doubling. The repetition frequency was measured to around 8.6 kHz with FWHM pulse durations of about 250 ns with a maximum average output power of about 100 mW and pulse peak power of around 36 W. The repetition frequency was lowered to 86 Hz by employing a tuned chopper.

During the frequency doubling of the pump laser, damaging of the KTP crystals used was observed already at intensities as low as 33 MW/cm^2, results that are in line with previous data from Boulanger *et al.* [26]. However, even lower damage thresholds with RKTP suggests that the damaging experienced is not a result of gray-tracking as proposed by Boulanger *et al.*, though further studies of the phenomenon would be required in order to draw any clear conclusions.

A laser cavity to manage FRET lasing was designed using a VBG to suppress lasing from the donor fluorophore. The cavity was constructed using a method developed to align a cavity, containing at least one VBG, prior to introducing the gain medium in the cavity.

The Venus YFP dye laser did not lase, most probably because the concentration and the purity of the Venus YFP solution was too low.

6.2 Future work

The next natural step of this project or other projects aiming at demonstrating FRET lasing would be to try to demonstrate fluorescent dye lasing using a fluorescent dye of higher concentration. Such a fluorescent dye would most surely have to be produced in an external facility specializing in providing highly concentrated protein solutions.

Another change that could fairly easily be implemented is to change the design of the FRET laser cavity. Instead of a four mirror cavity with an angled VBG, a two mirror cavity, similar to the one used by Gather and Yun [1], could be designed using a VBG with tailored properties. This should result in many advantages, such as easier aligning of the cavity, reduced cavity losses and better protein solution storage in the cavity. The comparatively high losses from the VBG would still be present, but with the intent of minimizing the stimulated emission from a future donor fluorophore the VBG is, to the best of my knowledge, a necessary part of the design.

References

[1] Malte C Gather and Seok Hyun Yun. Single-cell biological lasers. *Nature Photonics*, 5(7):406–410, 2011.

[2] Kensal E van Holde, W. Curtis Johnson, and Pui Shing Ho. *Principles of Physical Biochemistry*. Pearson Education, second edition, 1998.

[3] Elizabeth A Jares-Erijman and Thomas M Jovin. FRET imaging. *Nature biotechnology*, 21(11):1387–1395, 2003.

[4] Mark A Rizzo, Gerald H Springer, Butch Granada, and David W Piston. An improved cyan fluorescent protein variant useful for FRET. *Nature biotechnology*, 22(4):445–449, 2004.

[5] Orazio Svelto. *Principles of Lasers*. Springer Verlag, fourth edition, 1998.

[6] Anthony E. Siegman. *Lasers*. University Science Books, first edition, 1986.

[7] Jonas E Hellstrom, Björn Jacobsson, Valdas Pasiskevicius, and Fredrik Laurell. Finite beams in reflective volume Bragg gratings: theory and experiments. *Quantum Electronics, IEEE Journal of*, 44(1):81–89, 2008.

[8] Jun-Ya Hasegawa, Kazuhiro Fujimoto, Ben Swerts, Tomoo Miyahara, and Hiroshi Nakatsuji. Excited states of GFP chromophore and active site studied by the SAC-CI method: Effect of protein-environment and mutations. *Journal of computational chemistry*, 28(15):2443–2452, 2007.

[9] Abhijit K Das, Jun-Ya Hasegawa, Tomoo Miyahara, Masahiro Ehara, and Hiroshi Nakatsuji. Electronic excitations of the green fluorescent protein chromophore in its protonation states: SAC/SAC-CI study. *Journal of computational chemistry*, 24(12):1421–1431, 2003.

[10] Alexander A Voityuk, Maria-Elisabeth Michel-Beyerle, and Notker Rösch. Quantum chemical modeling of structure and absorption spectra of the chromophore in green fluorescent proteins. *Chemical physics*, 231(1):13–25, 1998.

[11] Jocelyn R Grunwell, Jennifer L Glass, Thilo D Lacoste, Ashok A Deniz, Daniel S Chemla, and Peter G Schultz. Monitoring the conformational fluctuations of DNA hairpins using single-pair fluorescence resonance energy transfer. *Journal of the American Chemical Society*, 123(18):4295–4303, 2001.

[12] Aude Villoing, Myriam Ridhoir, Bertrand Cinquin, Marie Erard, Luis Alvarez, Germain Vallverdu, Pascal Pernot, Regis Grailhe, Fabienne Mérola, and Helene Pasquier. Complex Fluorescence of the Cyan Fluorescent Protein: Comparisons with the H148D Variant and Consequences for Quantitative Cell Imaging. *Biochemistry*, 47(47):12483–12492, 2008.

[13] Roger Y Tsien. The green fluorescent protein. *Annual review of biochemistry*, 67(1):509–544, 1998.

[14] Colin Brownlee. Cellular calcium imaging: so, whats new? *Trends in cell biology*, 10(10):451–457, 2000.

[15] Takeharu Nagai, Keiji Ibata, Eun Sun Park, Mie Kubota, Katsuhiko Mikoshiba, and Atsushi Miyawaki. A variant of yellow fluorescent protein with fast and efficient maturation for cell-biological applications. *Nature biotechnology*, 20(1):87–90, 2002.

[16] Brian A Pollok and Roger Heim. Using GFP in FRET-based applications. *Trends in cell biology*, 9(2):57–60, 1999.

[17] Gert-Jan Kremers, Joachim Goedhart, Erik B van Munster, and Theodorus WJ Gadella. Cyan and yellow super fluorescent proteins with improved brightness, protein folding, and FRET Förster radius. *Biochemistry*, 45(21):6570–6580, 2006.

[18] Nathalie B Vicente, Javier E Diaz Zamboni, Javier F Adur, Enrique V Paravani, and Víctor H Casco. Photobleaching correction in fluorescence microscopy images. In *Journal of Physics: Conference Series*, volume 90, page 012068. IOP Publishing, 2007.

[19] SP Laptenok, IHM Van Stokkum, JW Borst, B Van Oort, AJWG Visser, and H Van Amerongen. Disentangling picosecond events that complicate the quantitative use of the calcium sensor YC3. 60. *The Journal of Physical Chemistry B*, 116(9):3013–3020, 2012.

[20] Joseph R. Lakowicz. *Principles of Fluorescence Spectroscopy*. Springer Verlag, third edition, 2006.

[21] Staffan Tjörnhammar. *Thermal properties of volume Bragg gratings and its implications on lasers*. Licentiate thesis, Royal Institute of Technology (KTH), 2013.

[22] Bj Jacobsson et al. Experimental and theoretical investigation of a volume-Bragg-grating-locked Yb: KYW laser at selected wavelengths. *Optics Express*, 16(9):6443–6454, 2008.

[23] George Patterson, Rich N Day, and David Piston. Fluorescent protein spectra. *Journal of Cell Science*, 114(5):837–838, 2001.

[24] DA Kleinman. Theory of second harmonic generation of light. *Physical Review*, 128(4):1761–1775, 1962.

[25] YF Chen and YC Chen. Analytical functions for the optimization of second-harmonic generation and parametric generation by focused Gaussian beams. *Applied Physics B*, 76(6):645–647, 2003.

[26] B Boulanger, MM Fejer, R Blachman, and PF Bordui. Study of KTiOPO 4 gray-tracking at 1064, 532, and 355 nm. *Applied physics letters*, 65(19):2401–2403, 1994.

[27] JP Feve, B Boulanger, G Marnier, and H Albrecht. Repetition rate dependence of gray-tracking in KTiOPO 4 during second-harmonic generation at 532 nm. *Applied physics letters*, 70(3):277–279, 1997.

[28] Andrius Zukauskas, Valdas Pasiskevicius, and Carlota Canalias. Second-harmonic generation in periodically poled bulk Rb-doped $KTiOPO_4$ below 400 nm at high peak-intensities. *Optics express*, 21(2):1395–1403, 2013.

[29] Igor V Ciapurin, Leonid B Glebov, and Vadim I Smirnov. Modeling of Gaussian beam diffraction on volume Bragg gratings in PTR glass. In *Integrated Optoelectronic Devices 2005*, pages 183–194. International Society for Optics and Photonics, 2005.